CENTRO DE INVESTIGACIONES
EN ÓPTICA, A.C.

Review in digitization of solids through structured light.

MAESTRÍA EN CIENCIAS (ÓPTICA)

Asesor: Dr. Manuel Servin Guirado

Estudiante: Ing. Jorge García Armenta

Octubre de 2015
León, Guanajuato, México

In loving memory of my grandfather Juan García.

ABSTRACT

The use of the fringe projection profilometry is a wide field of study in optical metrology, and it has been in constant development due to the recent progress in image sensors and computers. It has application in many scientific and engineering areas; being one of the most common the measurement of object's shape.

This thesis discusses in a brief way the theoretical background in fringe analysis and the most commonly used methods to retrieve the optical phase of an interferogram. Also, here were reviewed and implemented structured light techniques to reconstruct the shape of solids and have a digital model of them. The reviewed techniques were co-phase fringe projection, on-axis fringe projection and 3D shape measurement by line projection. Meanwhile the co-phase and line projection were replicated from previous works done by Servin *et al.*, the on-axis projection was done by using a novel configuration in this technique.

Moreover, as the final step in the fringe analysis is the phase unwrapping process, during this project was developed an algorithm, based in flood-fill scanning and quality-guided techniques, to make a continuous map of the object's estimated phase. This algorithm was tested on some phase maps in order to know its performance.

DEDICATIONS

To my parents Fernando and Eva Angelina.

I would like to thank you for all the unconditional support through my postgrad studies, and my studies in general since I was a child. To you is my greatest admiration and esteem. Without your help, motivation, advices, scolding, discipline and affection I wouldn’t be the person that I am now. From you I learned the desire to excel and to make always my best endeavor, fighting for always accomplish my goals. Thanks for everything.

To my brother and sister Fernando and Evangelina.

For all the unique experiences that we had lived since ever. I appreciate all the time that we spend together, even though that now we don’t see each other very often. I know that you always will be there for me and I will be there for you two. Because you are older than me, I can learn from your mistakes in advance, and for that I would like to thank you brothers.

To my grandparents Juan, Rosalva, Jorge and María Amparo.

Thanks for all the experiences that you have convey to me. You are a truly inspiration for your sons and all your grandsons. Your lives are great stories of happiness and success, always dedicated to the welfare of the family. Thank you all that advices that you had given to me.

ACKNOWLEDGES

To the Centro de Investigaciones en Optica for all the material and final support. For provide me of all the necessary equipment for my project and gave me a nice place to work and to develop my skills.

To my adviser Dr. Manuel Servin for all the help, teaching and support. For motivate my incursion in this science field of computer vision and fringe analysis. Also, for sharing your professional experiences with me and always advise me for a better professional future. Without your guidance this project wouldn't be possible.

To Dr. Moises Padilla for all the teaching and tuition during my learning in this new research field to me. Thanks for always been available whenever a problem appear in my research. Also, for all the advices and image examples that you provided for this dissertation. And finally for been my reviser for my work and correct for the best this document.

To Dr. Manuel de la Torre for helping me to make this a better thesis. For been my reviser and contribute with good ideas to my thesis.

To Lic. Guillermo Garnica for instruct me in the use of the instruments in the laboratory of digital image processing. For giving me advices and ideas in the development of the different setups for my research. For provide me of the materials that I needed and helping me during the realization of my master degree project.

To my generation's colleagues and friends Javier and Olivia, for all the good times and conversation that we had together. To make our study hours less tedious and more enjoyable, and always trying to help each other.

To my postgrad's friends and colleagues, especially Heriberto, Flor, Rodrigo and Carlos for all the memorable and fun events inside and outside of CIO. For all the meaningful talks and company during this two and a half years.

To the important persons in my life. Nadia, for all the support, love and motivation to get my degree. Alejandra for all your support, help, advices and great talks during my stay at CIO. To Giovani for the help getting me a place to stay during the admission test and interview, and also for all the company and good moments here at Leon and Guanajuato.

Finally, I would like to acknowledge CONCACYT for the financial support through this two years carrying out my master degree.

1. Structured light profilometry.

1.1- Introduction.

In the recent decades, the implementation of fringe projection techniques to reconstruct or generate the surface information of an object has become one active research area in optical metrology. The measurement of the three-dimensional shape of solids is called profilometry. Fringe projection profilometry techniques have many applications in science and engineering. For example, to monitor the manufacturing quality process of mechanical components, to measure the superficial stress or strain of deformable objects [1], to capture biometrical data like face recognition [2] or the 3D face reconstruction [3], application in computer vision [4], kinematic applications such as: the shape and position of a moving object/creature [5], reverse engineering to digitalize objects [6], quality control of printed circuit board manufacturing [7] and plays an important role in many other applications. A main advantage of optical profilometry is the non-contact nature of it.

Nowadays, the most common optical techniques for 3D shape measurements include the Digital Image Correlation (DIC), the laser scanning, structured light projection, Moiré and Electronic Speckle Pattern Interferometry (ESPI). Among them, the structured light projection consists of a structured pattern (such as a line or fringes) projected onto an object's surface. Due the object's surface geometry under study, the projected light pattern will be deformed when it is viewed from certain angle. The superficial information will be encoded in the deformed light pattern; therefore, one can decode this information to retrieve the phase of these captured images of the object. This technique has many advantages, it can works with opaque and reflective objects, it is cheaper compared with laser techniques setups, it is a full field measurement and the acquisition data can be done very fast due the use of CCD cameras and computers.

In this thesis, will be reviewed the art's state of the techniques of co-phase and line scanning, moreover is proposed a new setup for the on-axis fringe projection technique. Also, here is described a quality-guided flood-fill unwrap algorithm developed to create a smooth phase map of the captured interferograms.

This chapter briefly describes the basic concepts involved in the techniques of co-phase fringe projection, on-axis fringe projection y line projection. In the subsequent chapters it is described the theory behind these methods, and the experimental implementation of them.

1.2 Basic concepts of digital interferometry.

The digital interferometry is a combination between the classical optical interferometry and the computer-aided processing of digital fringe patterns. The techniques belonging to this hybrid field have been successfully developed helped with the progress in the computational areas, thanks to a major speed processing and data storage in the recent years. Besides, the use of digital image sensors like Charge-Coupled Device (CCD) and the Complementary Metal-Oxide Semiconductor (CMOS), add to this success.

An interferogram with a fringe pattern is defined as a cosine signal where a continuous map, corresponding to the physical quantity being measured, is phase-modulated by an interferometric system [8]. An ideal fringe pattern is mathematically described by

$$I(x,y) = a(x,y) + b(x,y)\cos[\varphi(x,y)] \tag{1.1}$$

where $\{x,y\} \in \mathbb{R}^2$; $a(x,y)$ is the background constant function of the fringes, $b(x,y)$ is the visibility of the fringes and $\varphi(x,y)$ is the searched phase function. To retrieve the phase $\varphi(x,y)$ is necessary to demodulate this fringe pattern.

Eq. (1.1) can be analyzed as an ill-posed inverse problem, where some kind of regularization is required to deal with the sign ambiguity of the cosine function (even function) and the 2π phase ambiguity, in order to obtain the correct phase estimation. Nevertheless, it is possible to visualize a solution to retrieve the phase of the fringe pattern. First, let's rewrite Eq. (1.1) in the complex representation of the cosine function.

$$I(x,y) = a(x,y) + \frac{1}{2}\, b(x,y)\left\{e^{[i\,\varphi(x,y)]} + e^{[-i\,\varphi(x,y)]}\right\} \tag{1.2}$$

If we eliminate the DC signal $a(x,y)$ and the term $e^{[-i\,\varphi(x,y)]}$ in Eq. (1.2), leaving just $\frac{1}{2}\, b(x,y)\left\{e^{[i\,\varphi(x,y)]}\right\}$, we have

$$\tan\hat{\varphi}(x,y) = \frac{\mathrm{Im}\left\{(1/2)b(x,y)e^{[i\,\varphi(x,y)]}\right\}}{\mathrm{Re}\left\{(1/2)\,b(x,y)\,e^{[i\,\varphi(x,y)]}\right\}} \tag{1.3}$$

where $b(x,y) \neq 0$ and $\hat{\varphi}(x,y)$ is the wrapped phase map searched ($\varphi(x,y) \bmod 2\pi$) by computing the arc-tangent of Eq. (1.3).

1.3 Interferogram types.

A fringe pattern could be seen as a system with three unknown variables in a single equation, however, in digital interferometry we are able to modify the pattern directly with software, adding known changes in the argument of the cosine signal in Eq. (1.1)

$$I(x,y,t) = a(x,y) + b(x,y)\cos[\varphi(x,y) + c(x,y,t)] \tag{1.4}$$

where $c(x,y,t)$ is a known function (typically a reference plane) and it is called the spatiotemporal carrier of the interferogram. This carrier can be adapted to obtain two types of interferograms with closed or open fringes.

Interferograms with open fringes, have the carrier $c(x,y,t)$ with spatial values and the temporal term is optional depending on the method to retrieve the optical phase (see chapter 3). For example, it can only have components on the x axis, then the Eq. (1.4) with this carrier will be

$$I(x,y,t) = a(x,y) + b(x,y)\cos[\varphi(x,y) + \omega_0 x] \tag{1.5}$$

where ω_0 is a known constant which gives the spatial frequency of the fringes in the reference plane.

An example of an open fringe pattern is shown in Fig. 1.1. Here is presented a simulation created in Matlab with the peaks function as the phase difference, with a spatial frequency of the fringes $\omega_0 = {}^{\pi}/_{4}$ and using a carrier of vertical fringes (just components in the x axis).

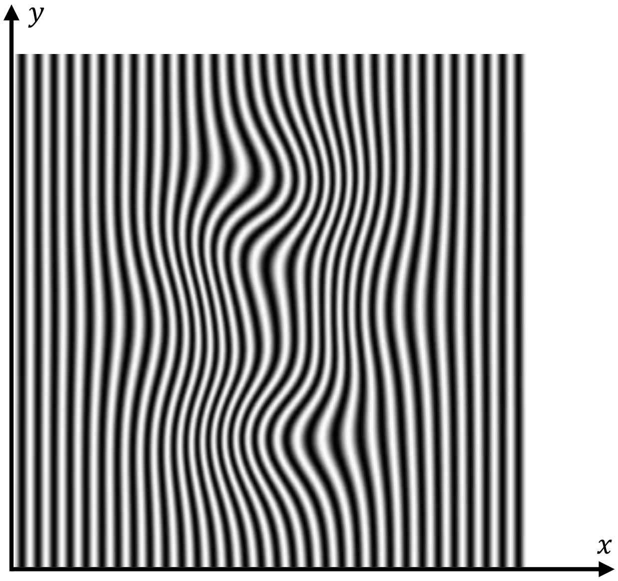

Fig. 1.1.-Simulation of an interferogram with open fringes with the "peaks" function of Matlab with a size of 256 x 256 pixels.

An important advantage of this kind of interferograms is that we only need one image to determine the phase map. One of the methods to do this is using the Fourier transform formalism proposed by *Takeda et al.* [9].

The other type of interferogram, called closed fringes, is obtained when the phase difference is just a cosine function without open lines and also the carrier can have temporal components to induce a shift in the phase, enabling the demodulation of the fringes. For example, a simulated closed fringes interferogram is shown in Fig 1.2. It was created with the same peaks function used in Fig 1.1, without a displacement in the phase.

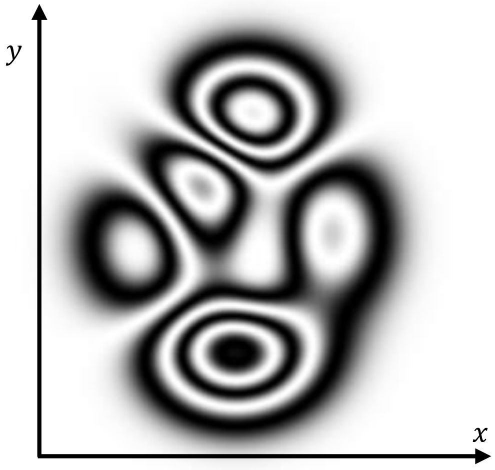

Fig. 1.2.-Simulation of a closed fringe interferogram (same dimension of Fig. 1.1).

The modulated phase map in this kind of interferogram can be obtained using the method of *Phase-Shifting Interferometry* (PSI). PSI is not limited to one kind of interferogram, is equally useful in open or closed fringes. In the PSI, a sequence of fringe patterns is generated introducing a linear shift in the cosine argument of the interferogram. The theoretical concepts of this method will be discussed on chapter 3.

1.4 Fringe projection profilometry.

The fringe projection profilometry is the measurement of the three dimensional object's phase through the use of a known pattern of structured light. However, the surface to measure needs to be diffusely reflective [12], because this technique is based on the projected light's reflection to the CCD camera. If the object doesn't reflect the light, the sensor won't capture any light's deformation data. Also, if the object creates shadows, the interferorgram phase will not be well defined in these areas. The Fig. 1.3 shows a typical fringe projection profilometry arrangement.

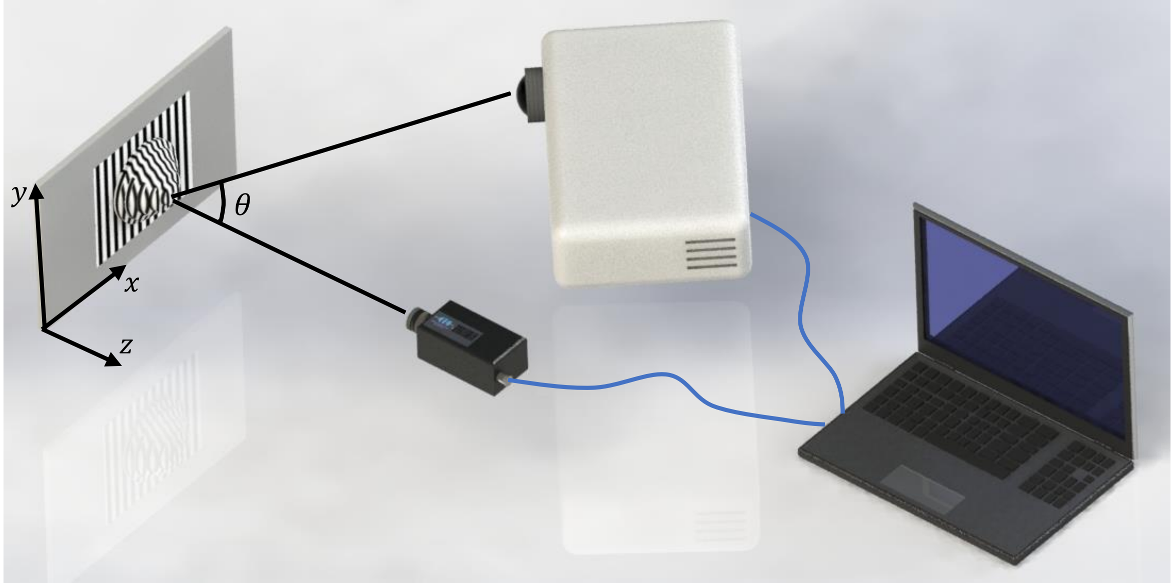

Fig. 1.3.-Fringe projection profilometry arrangement.

The system consists of: the object under study, a commercial projector, a camera viewing directly the object and a processing/analysis unit. Basically, to measure the shape through the fringe projection we need to project a structured light pattern onto the object surface, then we record the image of the fringe pattern that is phase-modulated by the different object's heights, the next step is to calculate the wrapped phase of the recorded image using a fringe demodulation method, then it is necessary to use an algorithm to unwrap the calculated phase and finally calibrate the system for mapping the unwrapped phase distribution to real world 3-D coordinates.

These techniques of profilometry are triangulation-based, either the surface points of the object are recorded from two different views, or a structured light pattern is projected from one direction and observed from another (Fig. 1.3). The angle between these two directions (θ) is used to calculate the 3-D coordinates of the object surface points.

Fig. 1.4 shows a fringe projection profilometry's geometry with crossed-optical-axes [10], this means that the optical axes $E'_p\, E_p$, of a projector lens, crosses the optical axis $E'_c\, E_c$ of a camera lens at point 0 on a fictitious reference plane R normal to the camera axis, serves as reference from which the object height $h(x, y)$ is measured.

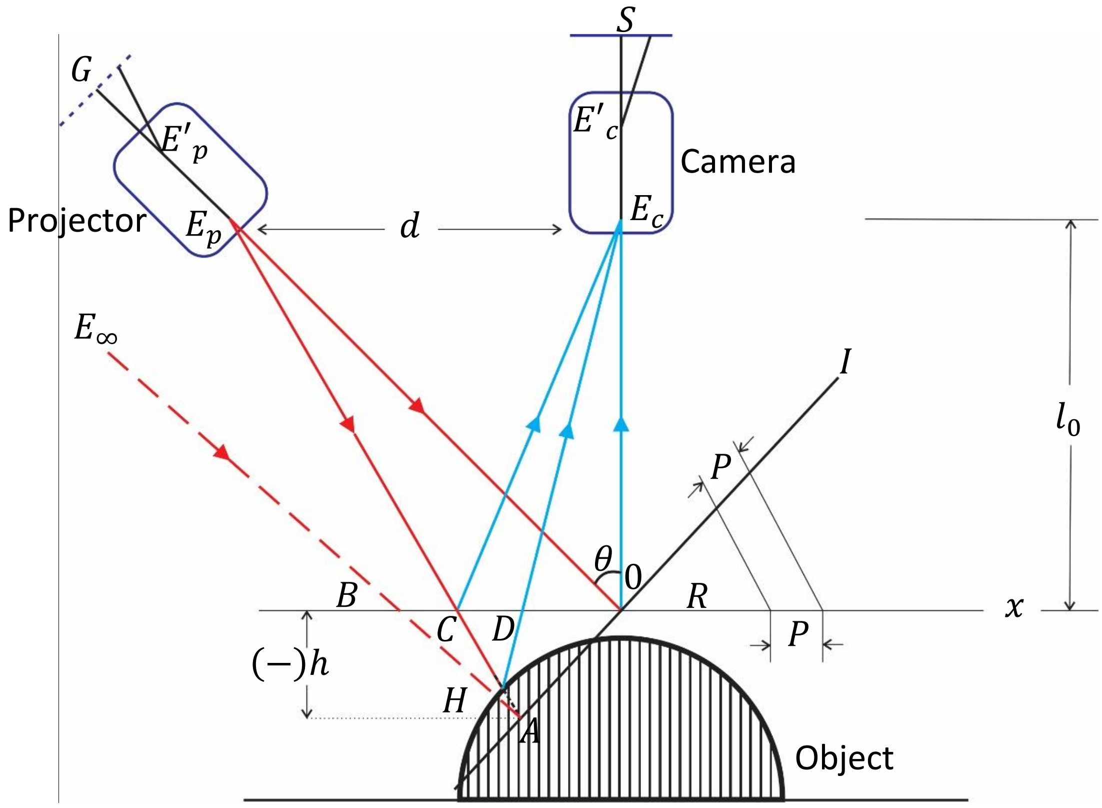

Fig. 1.4.-Crossed-optical-axes geometry.

The distance between the camera and the projector is defined as d. l_0 is the distance from the camera's plane to the plane *R.* The projected fringes are normal to the plane of the figure, and its conjugate image is formed by the projector lens (plane *G*) on the plane I through the point 0; the entrance and exit pupils of the projector lens are denoted by E_p and E'_p respectively. E_c and E'_c are the centers of the entrance and exit pupil of the camera lens, which form the image reference plane R onto the sensor plane S. If there isn't an object, or the object is flat (an uniform plane on R), the height $h(x, y)$ would be 0. If E_p is at infinity (denoted by E_∞ in the telecentric case), the image projected on the object surface, and observed through point the E, is a regular fringe pattern which can be modeled by a Fourier series expansion

$$g_T(x, y) = \sum_{n=-\infty}^{\infty} A_n \exp[2\pi i n f_0 x] \, , \tag{1.6}$$

Where A_n is the amplitude of the projected grating and the fundamental frequency f_0 of the observed grating image is defined as

$$f_0 = 1/P = \cos(\theta/_P) \tag{1.7}$$

where *P* is the period of the grating.

We define the deformed grating image for $h(x,y)=0$ as

$$g_0(x,y)=\sum_{n=-\infty}^{\infty} A_n \exp\{2\pi i n f_0[x+s_0(x)]\}, \tag{1.8}$$

where $s_0(x)=\overline{BC}$ is a function of x and has a positive sign when the projector is at the left of the setup (Fig. 1.4). Expressing eq. (1.8) as a spatially phase-modulated signal we get

$$g_0(x,y)=\sum_{n=-\infty}^{\infty} A_n \exp\{i[2\pi n f_0 x+n\varphi_0(x,y)]\}, \tag{1.9}$$

where the initial phase modulation φ_0 is

$$\varphi_0(x)=2\pi f_0 s_0(x)=2\pi f_0\overline{BC}. \tag{1.10}$$

Similarly, for a general object $h(x,y)\neq 0$, the principal ray $\overline{E_pA}$ is propagated to the object surface at point H:

$$g_0(x,y)=\sum_{n=-\infty}^{\infty} A_n \exp\{i[2\pi n f_0 x+n\varphi(x)]\}, \tag{1.11}$$

where

$$\varphi(x,y)=2\pi f_0 s(x,y)=2\pi f_0\overline{BD}. \tag{1.12}$$

Now, we can calculate the object-height distribution $\Delta\varphi$ by the difference between eqs. (1.10) and (1.12) as,

$$\begin{aligned}\Delta\varphi(x,y)&=\varphi(x,y)-\varphi_0(x,y)\\&=2\pi f_0(\overline{BD}-\overline{BC})=2\pi F_0\overline{CD}.\end{aligned} \tag{1.13}$$

According to the derivate formula to convert the measured phase distribution into the physical height distribution (made by *Takeda et al* [7]), the vector $\overline{CD}$ is defined as

$$\overline{CD}=-dh(x,y)/[l_0-h(x,y)], \tag{1.14}$$

where the object height $h(x,y)$ is defined positive above the reference plane R. Substituting eq. (1.14) into Eq. (1.13) and solving it for $h(x,y)$, we obtain the conversion formula

$$h(x,y)=\frac{l_0\Delta\varphi(x,y)}{[\Delta\varphi(x,y)+2\pi f_0 d]}. \tag{1.15}$$

In linear calibration methods of fringe projection setups, we can assume that l_0 is much larger than h, so eq. (1.17) can be approximated with linear relation [11] as follow

$$h(x,y)=\frac{l_0\Delta\varphi(x,y)}{2\pi f_0 d}=K(x,y)\,\Delta\varphi(x,y), \tag{1.16}$$

where $K(x, y)$ is a function called the calibration coefficient with spatial coordinates (x, y), and is decided by the parameters of the optical setup. For more information see reference [10].

There are several available methods to obtain the object's height profile from the deformation of a projected fringe pattern seen over the surface. Fig. 1.5 presents an organized scheme of some methods used in profilometry.

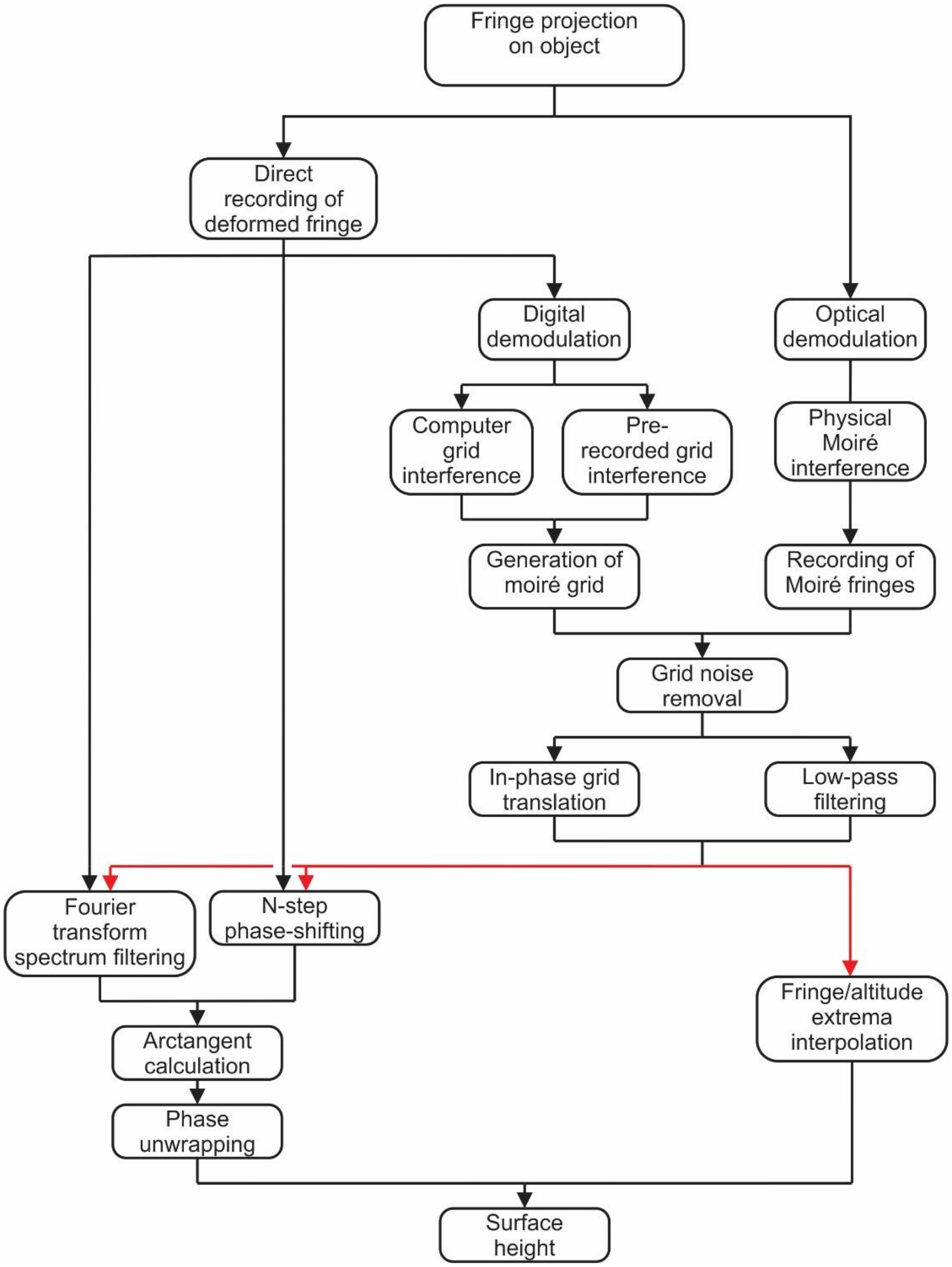

Fig. 1.5.-Schematic diagram of the 3 main profilometry techniques [12].

The simplest optical setup for grid projection profilometry, is the use of a single projector and a camera placed at a fixed angle respect to the projector direction. This technique corresponds to the left side of the scheme in Fig 1.5. However, this direct recording requires a camera resolution two times bigger than that of the projector's resolution, in order to fulfill the Nyquist-Shannon theorem. This means, that the camera must be capable to resolve the individual grid lines without aliasing effects between the grid lines and the camera pixels.

In the right side of Fig. 1.5, we can see the so called *Moiré profilometry*. In this case, the image of a grid is projected onto the surface of an object, but now the deformed grid lines are observed through an identical second straight grid, then a CCD camera is employed to record a series of images of the deformed grid from the object. However, this thesis will analyze only the techniques of direct recording of fringe projection.

2. DIGITAL SIGNAL PROCESSING (DSP)

The fringe images captured by the CCD camera in pixel arrays are discrete signals as the digital filters used in profilometry. In order to understand the fringe analysis it is necessary to know some fundaments of DSP and the linear systems theory. In this chapter the mathematical representation is introduced and the description of discrete signals and systems, and finally as the analysis of discrete systems.

2.1. Discrete-time signal and systems.

A signal is a function that represents a variable or physical quantity, and the independent variable of the mathematical representation of this signal can be either continuous or discrete. *Discrete-time signals* such as $x(n)$, where n is an integer, are defined at discrete times and then the independent variable takes only discrete values [13]; this means that this kind of signals are expressed as a number sequence. Each number represents the magnitude of the signal at certain time. In addition, the amplitude signal could be continuous or discrete. Digital signals are those where the time and the amplitude are discrete.

There are two ways to define a discrete-time signal $x(n)$; we can specify a rule to calculate de n^{th}value of the sequence or we can just explicitly list the values of the sequence.

Fig. 2.1(a) shows a sequence known as the *unite impulse* (or Dirac delta), $\delta(n)$, and it's defined as follows,

$$\delta(n)=\begin{cases}1 & n=0\\ 0 & n\neq 0.\end{cases} \tag{2.1}$$

Similarly, the shifted unit impulse sequence $\delta(n-k)$ (see Fig. 2.1 b) is defined with values in k as,

$$\delta(n-k)=\begin{cases}1 & n=k\\ 0 & n\neq k\end{cases}. \tag{2.2}$$

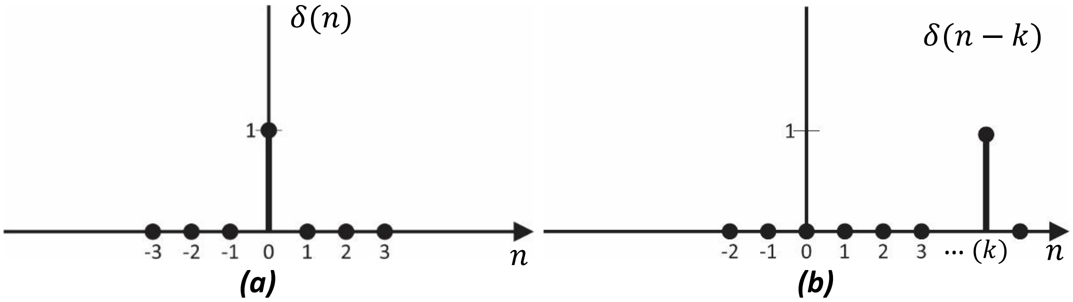

Fig. 2.1.-(a) unit impulse sequence, (b) shifted unit impulse sequence.

Another important discrete signal in DSP is the *Dirac comb* $\mathrm{III}(n)$, which is a periodic distribution of Dirac delta functions that plays an important role when signals are sampled, and it is defined as

$$\mathrm{III}(n) = \sum_{k=-\infty}^{\infty} \delta(n-k). \tag{2.3}$$

which is shown in Fig. 2.2.

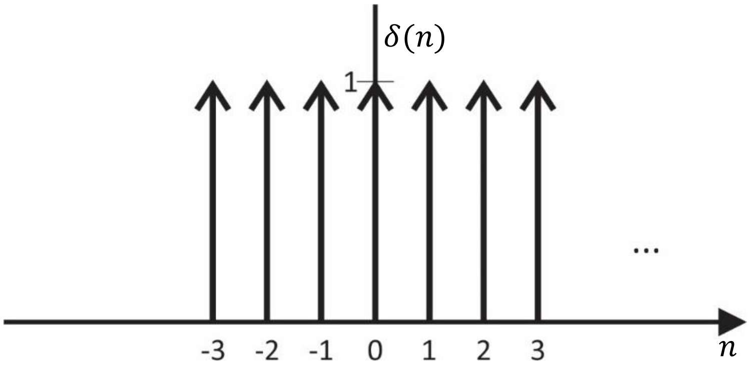

Fig. 2.2.-Dirac comb or sampling function.

Besides signals, the systems can also be continuous or discrete. A *discrete-time system* is a device or algorithm that operates on a discrete-time signal, called the input $x(n)$, according to some well-defined rule, to generate another discrete-time signal called output $f(n)$ or response of the systems [14]. We can express the transformation of $x(n)$ by the system into $f(n)$ with the following mathematical relation

$$f(n) = T[x(n)] \tag{2.4}$$

where the operator T denotes the transformation of $x(n)$ into $f(n)$, and it is often depicted as Fig. 2.3 shows.

Fig. 2.3.-Representation of a transformation that maps an input sequence $x(n)$ into an output sequence $f(n)$.

2.2. Linear time-invariant (LTI) systems.

A system that fulfill the superposition principle and its input-output characteristics do not change over time, is called a *linear time-invariant system* (LTI).

These LTI systems are defined by the principle of superposition (additivity and scalability). If $f_1(n)$ is the output to the input $x_1(n)$, and $f_2(n)$ is the corresponding output to $x_2(n)$, then a system is linear if and only if,

$$T[ax_1(n) + bx_2(n)] = aT[x_1(n)] + bT[x_2(n)] = af_1(n) + bf_2(n), \tag{2.5}$$

where a and b are arbitrary constants.

A system is called time-invariant if a time shift in the input signal causes the same time shift at the output signal. If the input introduces a delay k, this same delay will be at the output. Therefore, a system is time-invariant if

$$T[x(n-k)] = f(n-k). \tag{2.6}$$

To describe LTI systems, it is necessary to define the arbitrary discrete equation. It can be expressed as a sum of scaled, shifted (or delayed) unit samples as shown in the next equation

$$x(n) = \sum_{k=-\infty}^{\infty} x(k)\delta(n-k). \tag{2.7}$$

This representation in Eq. (2.7) together with the superposition principle and the time-invariance property, suggest that any LTI system is completely characterized by its unit sample response $h(n)$. Being $h(n)$ the response of the system to $\delta(n)$, then Eq. (2.7) for a LTI system becomes

$$f(n) = \sum_{k=-\infty}^{\infty} x(k)h(n-k). \tag{2.8}$$

The Eq. (2.8) is commonly called the convolution sum. Where $f(n)$ is an output sequence whose values are related to the values of the sequences $x(k)$ and $h(n)$, then $f(n)$ is the convolution of $x(n)$ with $h(n)$, denoted by the following notation,

$$f(n) = x(n) * h(n). \tag{2.9}$$

2.3. Digital sampling.

Usually one of the first steps in the fringe pattern analysis is to perform an analog-to-digital (A/D) conversion, called digital sampling. Sampling is the conversion of an analog signal into a discrete-time signal, obtained by taking “samples” of a continuous-time signal at discrete-time instants. Thereby, if $x(t)$ is the continuous-time input signal, the output is $x(nT) \equiv x(n)$, where T is the sampling interval.

Under the assumption that the temporal width (nT) of each sample approaches to zero, these samples can be represented as a sequence of unit impulse functions. Then, to do the sampling process let’s consider a continuous-time signal $x(t)$ being sampled into a discrete signal $x(n)$, having,

$$x(t)\mathrm{III}(t) = \{x(n)\} = \sum_{n=-\infty}^{\infty} x(n)h(t-n), \tag{2.10}$$

where $x(n) = x(t)|_{t=n}$ and $n \in \mathbb{R}$. Basically, the sampled signal is a composition of an impulse function series evenly spaced, weighed by the values of the original signal at the sampling instants. To visualize the sampling process, consider a sinusoidal continuous-time signal $x(t)$ and its discrete-time form of this signal $x(n)$, as seen in Fig. 2.4.

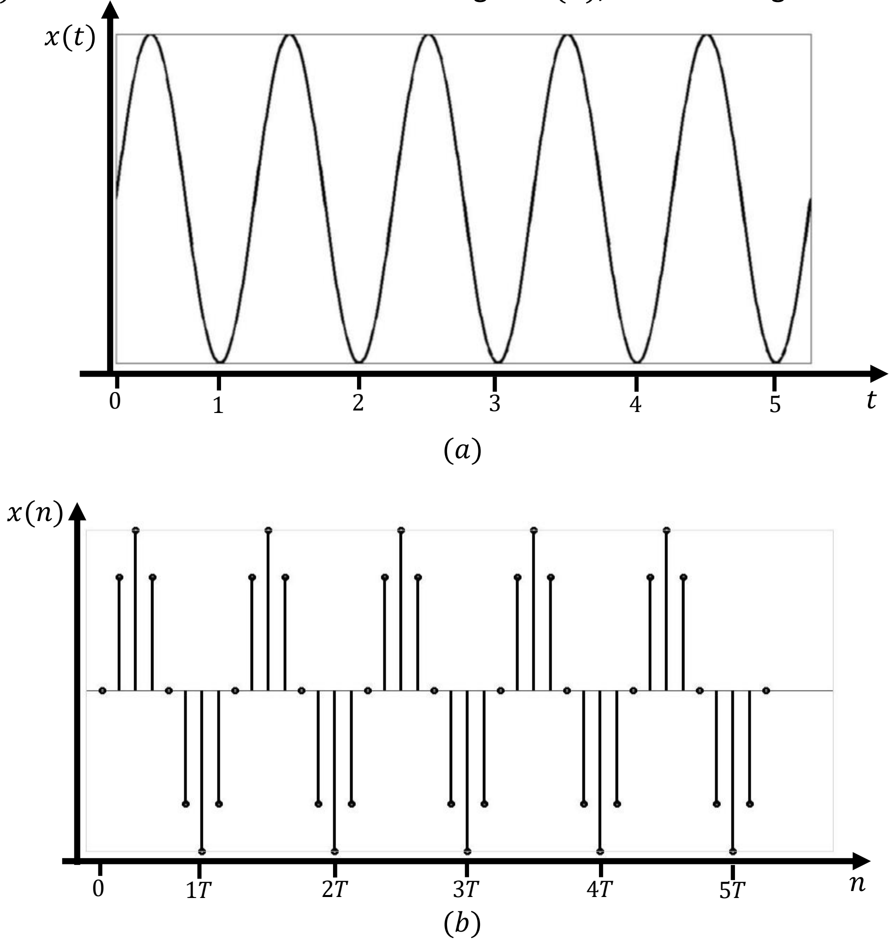

Fig. 2.4.-(a) Continuous-time sinusoidal signal $x(t)$. (b) Discretized signal $x(n)$ retrieved with Eq. (2.10).

To recover the continuous signal without information lost we need to fulfill certain conditions during the sampling process. Such as the Nyquist-Shannon sampling theorem. The first part of this theorem states that a band-limited signal $x(t)$, which maximum frequency is F_0, is completely determined by its sample values if the sampling frequency F_s is greater than twice the bandwidth of $x(t)$. Mathematically is defined as

$$F_s > 2F_0, \tag{2.11}$$

where $2F_0$ is the sampling rate known as *Nyquist rate*.

The second part of the Nyquist-Shannon theorem states that the continuous signal $x(t)$ can be reconstructed from its discrete samples $\{x(n)\}$ using the next interpolation function

$$x(t) = \sum_{n=-\infty}^{\infty} x(n) \frac{\sin(\pi t)}{\pi t}. \tag{2.12}$$

The function above means that under certain conditions, the continuous and the discrete signal contain the same information.

2.4. Frequency analysis of discrete-time signals.

One of the most useful mathematical tools in the signal and system analysis are the Fourier transform and the Fourier series. These representations involve the decomposition of the signal in terms of sinusoidal or complex components. With that term expansion, a signal is said to be represented in the frequency domain.

2.4.1. Discrete-time Fourier Transform (DTFT).

The frequency analysis of discrete-time finite-energy signals involves a Fourier transform in the time-domain. Thereby, the Fourier transform of these kind of signals $x(n)$ is defined as

$$X(\omega) = \sum_{n=-\infty}^{\infty} x(n) e^{-i\omega n}. \tag{2.13}$$

Physically, $X(\omega)$ represents the frequency contents of the discrete-time signal $x(n)$. This means that $X(\omega)$ is the representation of $x(n)$ into its frequency components. The frequency range of a discrete-time signal is unique over the frequency interval of $(-\pi, \pi)$ or, equivalently $(0,2\pi)$.

Uniform convergence is guaranteed if the discrete sequence $x(n)$ is absolutely summable.

That is

$$\sum_{n=-\infty}^{\infty} |x(n)| < \infty. \tag{2.14}$$

Hence Eq. (2.14) is a sufficient condition for the existence of the discrete-time Fourier transform (DTFT).

2.4.2. Frequency transfer function (FTF) of a LTI system.

As it was discussed in section 2.2, a LTI system is completely characterized by its impulse response function $h(t)$. Therefore, for every input $I(t)$, the corresponding output $f(t)$ is given by the next expression

$$f(t) = I(t) * h(t), \tag{2.15}$$

where the symbol * denote the convolution between the input $I(t)$ and the impulse response function $h(t)$. If we take the Fourier transform of Eq. (2.15), we get

$$F(\omega) = I(\omega)H(\omega). \tag{2.16}$$

$H(\omega)$ is the Fourier transform of the impulse response function, and it is known as the *Frequency Transfer Function* (FTF). It can be expressed as the relation

$$H(\omega) = \frac{F(\omega)}{I(\omega)} \tag{2.17}$$

With the condition that there is an input in the systems, or $I(\omega) \neq 0$. By the properties of the Fourier transform, the spectrum $H(\omega)$ is a complex-valued function, represented as,

$$H(\omega) = Re\{H(\omega)\} + i\, Im\{H(\omega)\}. \tag{2.18}$$

A complex function can also be represented in terms of its amplitude and phase, as

$$|H(\omega)| = \sqrt{Re\{H(\omega)\}^2 + Im\{H(\omega)\}^2}. \tag{2.19}$$

Meanwhile, the phase (mod 2π) of the function is given by

$$angle[H(\omega)] = \tan^{-1}\left[\frac{Im\{H(\omega)\}}{Re\{H(\omega)\}}\right]. \tag{2.20}$$

Some advantages to represent the FTF in terms of its amplitude and phase are [8]:

- The amplitude of the FTF is time-invariant:

$$\begin{aligned} &\mathcal{F}\{h(t+t_0)\} = H(\omega)e^{-i\omega t_0}, \\ &\left|H(\omega)e^{-i\omega t_0}\right| = |H(\omega)|\left|e^{-i\omega t_0}\right| = |H(\omega)|. \end{aligned} \tag{2.21}$$

- Plotting the magnitude $|H(\omega)|$, shows the frequency at which the system has null response (the zeros of the function).

$$|H(\omega_0)| = 0 \quad \Leftrightarrow \quad Re\{H(\omega_0)\} = Im\{H(\omega_0)\} = 0. \tag{2.22}$$

2.5. Convolution-based linear filters.

Filtering is an important process in objects digitization because it reduces the noise level in interferograms. The unwrapped phase of an interferogram is calculated with less errors if the retrieve wrapped phase of the interferogram is a smooth phase map.

There are two types of digital linear filters in DSP: Finite Impulse Response (FIR) filter and Infinite Impulse Response (IIR) filter.

For a FIR filter, the output is a convolution adding of the current value and a finite number of the previous values of the input (Fig. 2.5). We can express this by the following equation:

$$f(t) = \sum_{n=0}^{N} b_n I(t-n) = I(t) \sum_{n=0}^{N} b_n \delta(t-n), \tag{2.23}$$

where N is the filter order, $I(t)$ is the input signal, $f(t)$ is the output signal, and b_n are the filter coefficients. Therefore, the impulse response $h(t)$ of a FIR filter is given by

$$h(t) = \sum_{n=0}^{N} b_n \delta(t-n). \tag{2.24}$$

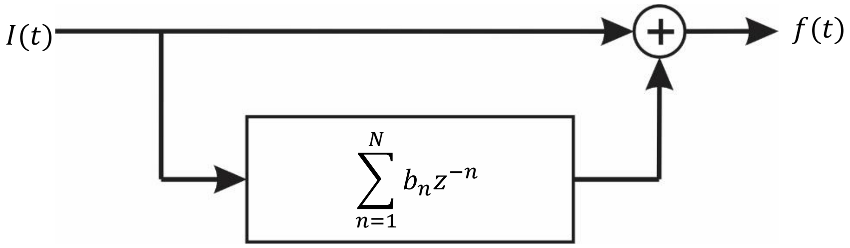

Fig. 2.5.-Block diagram for a Finite Impulse Response (FIR) filter.

For an IIR filter, the output at any time is given by a weighted addition of the current input and output, and a finite number of previous values of the input and the output, as shown in Fig. 2.6. We can describe this filter by doing two convolutions, one using the input and another using the output, as follow

$$\sum_{n=0}^{Q} a_n f(t-n) = \sum_{m=0}^{P} b_m I(t-n), \tag{2.25}$$

where P and Q are the feed-forward and the feed-back filter order respectively, while a_n and b_m are the feed-back and feed-forward filter coefficients respectively.

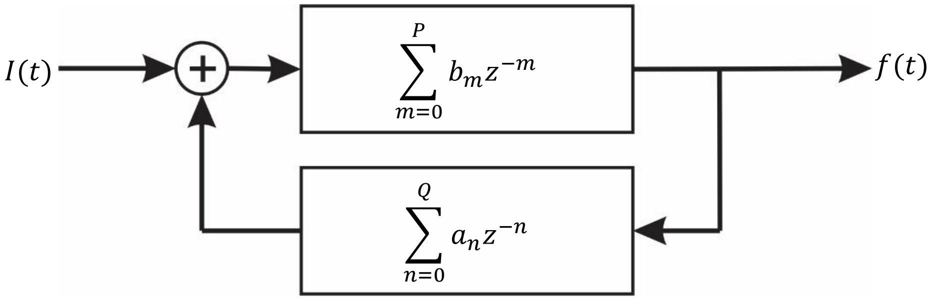

Fig. 2.6.-Block diagram of an Infinite Impulse Response (IIR) filter.

In the fringe pattern analysis, the input data are discrete arrays that depend on two independent variables (x and y). In general, the fringe patterns contain a low-frequency signal along with a high-frequency noise. Then, we need to implement a low-pass filter in order to remove a substantial amount of noise, making the demodulation process more reliable. In contrast with the 1-D filters described before, we need a 2-D filter generalizing the filters IIR and FIR. To analyze the 2-D filter in the frequency domain, we need to define the direct formula for the 2D Fourier transform and 2D Z-transform, that are

$$\mathcal{F}\{f(x,y)\} = F(u,v) = \iint f(x,y)e^{-i(ux+vy)}dxdy, \tag{2.26}$$

$$Z\{f(x,y)\} = F(z_x, z_y) = \sum_{n=-\infty}^{\infty}\sum_{m=-\infty}^{\infty} f(n,m)z_x^{-n}z_y^{-m}. \tag{2.27}$$

The 2D DTFT is calculated evaluating the Eq. (2.27) in $z_x = e^{iu}$ and $z_y = e^{iv}$, then we obtain

$$\mathcal{F}\{f(n,m)\} = F(u,v) = \sum_{n=-\infty}^{\infty}\sum_{m=-\infty}^{\infty} f(n,m)e^{-i(nu+mv)}. \tag{2.28}$$

Where $f(n,m) = f(x,y)|_{(x,y)=(n,m)}$. With digital systems the equations that we are going to use are Eq. (2.27) and Eq. (2.28).

2.6. Regularized spatial linear filtering techniques.

Many problems in fringe analysis are formulated as function of interpolation or approximation, where the target functions needs to be smooth a priori. In order to suppress the noise on a fringe pattern we can apply a regularization filter. A common example for classical regularization is the low-pass filtering. According to *Marroquin et al.* [15], it can be defined as: given the signal $I(x,y)$, find a smooth function $f(x,y)$ defined on a two dimensional field L, which may be modeled by

$$I(x,y) = f(x,y) + n(x,y), \ \ \forall (x,y) \in S, \tag{2.29}$$

where $n(x,y)$ is a high-frequency noise field, and S is the subset of L where the signals functions have a good signal-to-noise ratio. The low-pass filtering process is an optimizing inverse problem, where one need to maintain a compromise between obtaining a smooth filtered field $f(x,y)$ and keeping a good fidelity of the observed data $I(x,y)$.

In the discrete form, the low-pass filtering regularization can be defined as a minimization of energy functionals. The functions $f(x,y)$ and $I(x,y)$ are defined on the nodes of a regular lattice L inside of a sum over the domain of interest and it can be mathematically expressed as

$$U[f(x,y)] = \sum_{(x,y)\in S} \{[f(x,y) - I(x,y)]^2 + \eta R[f(x,y)]\}, \tag{2.30}$$

where S is the subset of L where the observations are available. There are two varieties of regularization filters or energy functionals; one is called *first-order membrane regularizer* and it corresponds to the mechanical energy of a 2D membrane $f(x,y)$, attached by linear springs to the observations $I(x,y)$, the other energy functional is constructed using a second-order or *metallic thin-plate regularizer*. Both optimizing systems are compared in Fig. 2.7.

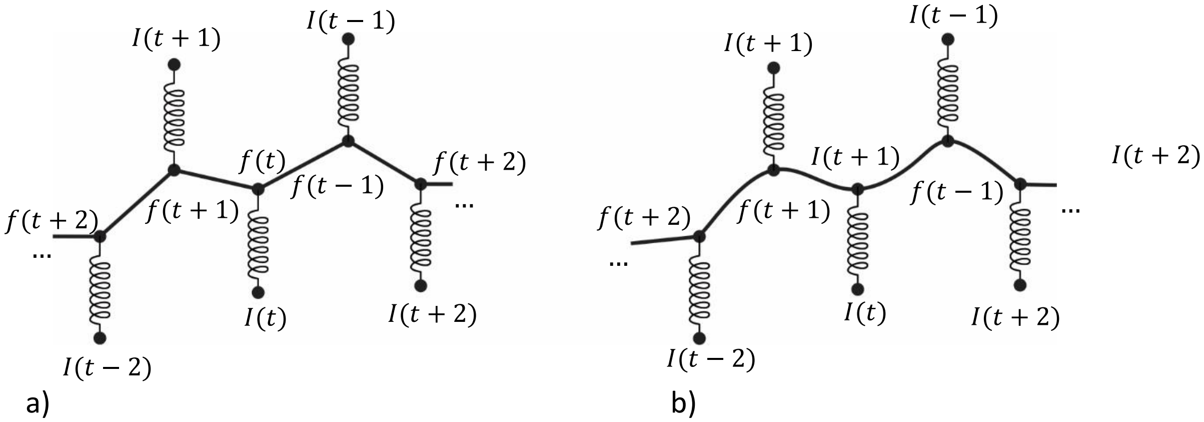

Fig. 2.7. - Horizontal slice diagram of the estimated fields obtained with a) first-order membrane and b) second-order metallic thin-plate regularizers.

The first order regularizer $R_1\ [f(x,y)]$ may be approximated by

$$R_1[f(x,y)] = [f(x,y) - f(x-1,y)]^2 + [f(x,y) - f(x,y-1)]^2, \tag{2.31}$$

and the metallic thin-plate regularizer $R_2[f(x,y)]$ may be approximated by

$$\begin{aligned} R_2[f(x,y)] = {} & [f(x+1,y) - 2f(x,y) - f(x-1,y)]^2 \\ & + [f(x,y+1) - 2f(x,y) - f(x,y-1)]^2 \\ & + [f(x+1,y+1) - f(x-1,y-1)]^2 \\ & + [f(x-1,y+1) - f(x+1,y-1)]^2. \end{aligned} \tag{2.32}$$

A simple way to optimize the above discrete energy functionals is by gradient descent, approaching the first iteration of $f(x,y)$ as the obervations $I(x,y)$, that is

$$\begin{aligned} & f^0(x,y) = I(x,y), \\ & f^{k+1}(x,y) = f^k(x,y) - \mu \frac{\partial U[f(x,y)]}{\partial f(x,y)}, \end{aligned} \tag{2.33}$$

where k is the iteration number and $\mu \ll 1$ is the step size of the gradient search.

In order to do a practical implementation of this regularization, we need to create a mask m. The mask specifies the valid pixels, in the fringe pattern, that need to be filtered and also to denote the interest region of our image. So, defining the function $m(x,y)$ in the lattice L with $N \times M$ nodes, we have

$$m(x,y) = \begin{cases} 1 & \forall (x,y) \in S \\ 0 & otherwise. \end{cases} \tag{2.34}$$

Using this mask in Eq. (2.30) for a first-order regularizer, the filtering problem can be defined as

$$U[f(x,y)] = \sum_{x=0}^{N-1} \sum_{y=0}^{M-1} \{[f(x,y) - I(x,y)]^2 m(x,y) + \eta R[f(x,y)]\}, \tag{2.35}$$

where

$$\begin{aligned} R[f(x,y)] = {} & [f(x,y) - f(x-1,y)]^2 m(x,y) m(x-1,y) \\ & + [f(x,y) - f(x,y-1)]^2 m(x,y) m(x,y-1). \end{aligned} \tag{2.36}$$

Then the partial derivative of the energy functional is calculated as

$$\begin{aligned} \frac{\partial U[f(x,y)]}{\partial f(x,y)} = {} & [f(x,y) - I(x,y)] m(x,y) \\ & + \eta [f(x,y) - f(x-1,y)] m(x,y) m(x-1,y) \\ & - \eta [f(x+1,y) - f(x,y)] m(x,y) m(x+1,y) \\ & + \eta [f(x,y - f(x,y-1)] m(x,y) m(x,y-1) \\ & - \eta [f(x,y) - f(x,y+1)] m(x,y) m(x,y+1) \end{aligned} \tag{2.37}$$

The mask $m(x, y)$ is the function that decouples valid fringe data for its surrounding background. This means that only the terms within the region of valid data, marked by $m(x, y)$, survive.

To compare the low-pass filter first-order membrane and the second-order metallic thin-plate, below is a numerical simulation of a masked wrapped phase with a distributed Gaussian noise. Fig. 2.8 (a) shows the noisy wrapped phase of a simulated interferogram, Fig. 2.8 (b) and Fig. 2.8 (c) shown the same wrapped phase after applying the filters of first and second order respectively

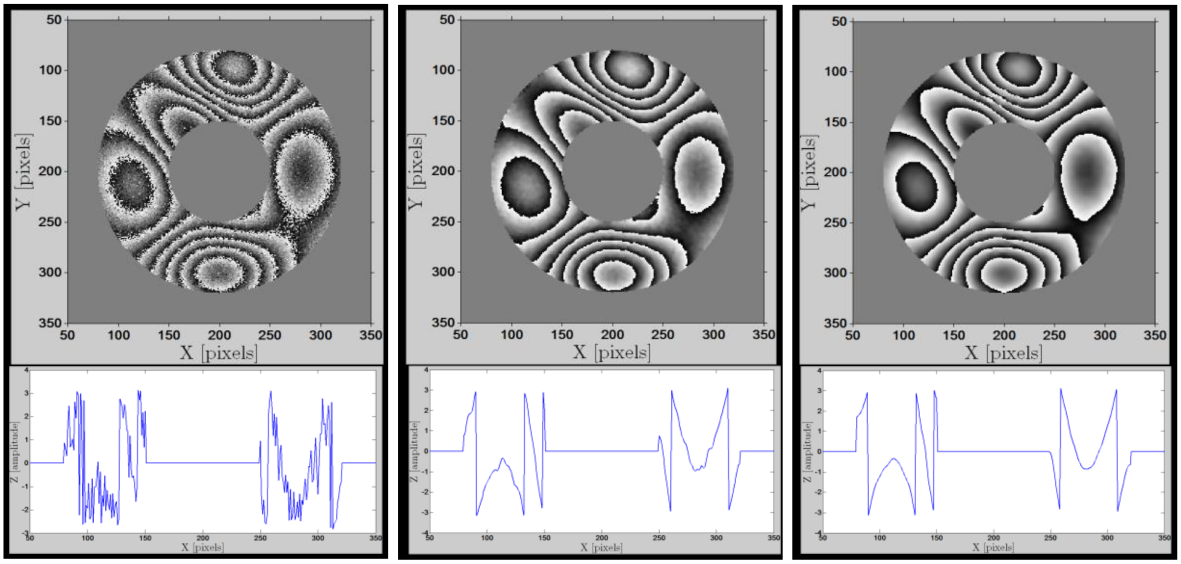
(a) Original data

(b) first-order membrane filter

(c) second-order metallic thin-plate filter

Fig. 2.8.-Qualitative comparison of the first-order membrane filter against second-order thin-plate filter with a transversal cut of the phase map in $y = 200$. (a) Noisy wrapped phase bounded by two circular pupils. In panel (b) we have the filtered phase using the first-order membrane. In panel (c) is shown the filtered phase using a second-order thin-plate filter.

The purpose to use a circular pupil is to confirm the efficiency of the regularized filters on the valid data, this means that these filters work only in the areas outside the mask $m(x, y)$. Note that both regularized filters in Fig. 2.8 b and c keep separate the pixels with valid phase data from those of the background denoted by the pupil.

Observing Fig. 2.8 (b) and (c) it is evident the difference between the firs-order filter against the second-order filter. With the second-order thin-plate filter is possible to get a smoother phase map in comparison with the first-order one. Also, due to the second-order nature of the thin-plate filter, the borders of the mask $m(x, y)$ can be extended to one pixel before and after of each axis, this can be seen in the Eq. (2.37) and in the filtered phase cut in Fig. 2.8.

3. Fringe pattern analysis.

The fringe analysis extracts relevant measurement data of the fringe patterns. Commonly it consists in methods of phase detection and fringe amplitude extraction. This chapter discusses about the methods for fringe demodulation used in the profilometry techniques implemented in this project, particularly the Fourier and the phase-shifting methods.

3.1. Fringe pattern demodulation.

The mathematical model of a fringe pattern (Eq. 1.1), is an amplitude and frequency modulated function (AM-FM). The objective of the fringe pattern analysis is to extract the amplitude and phase modulation, $A_0(x,y)$ and $\varphi(x,y)$ respectively, this process is also known as demodulation of the signal. One can add some *a priori* information to the argument of the cosine signal, in order to simplify the extraction of the amplitude and phase of the analytic signal. This addition to the argument of the original signal is known as *carrier*, and it can be either spatial or temporal. In the next topic, there is a description of some useful carriers and their possible application.

Fig. 3.1 shows a schematic diagram of the most used demodulation methods in digital interferometry. In the further sections we are going to focus our attention on the methods that used spatial carrier (single image) and the ones with temporal carrier (multiple images).

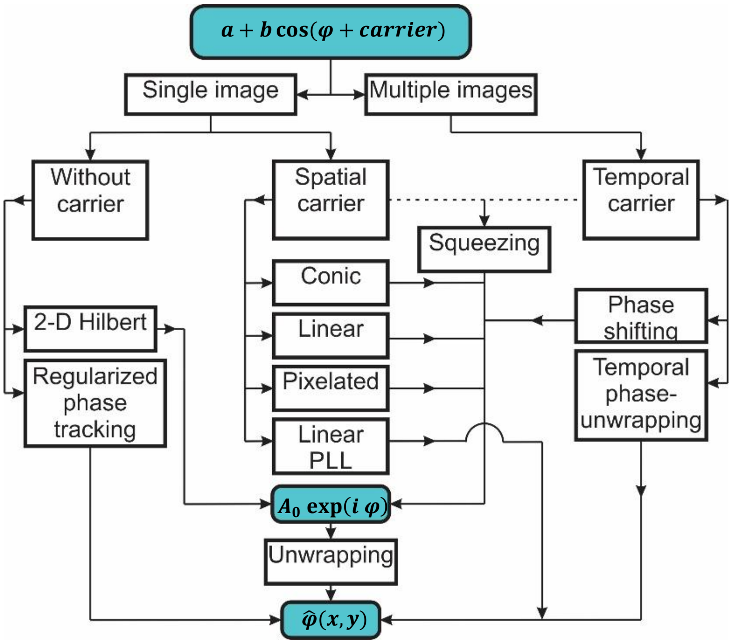

Fig. 3.1.- Schematic classification of the most common phase estimation methods in modern fringe pattern analysis.

The term $A_0\exp(i\varphi)$, in the figure above, is the isolated analytic signal from where we can straightforwardly compute the searched wrapped phase $\hat{\varphi}(x,y)$.

3.1.1. Fringe pattern carriers.

Carriers are known changes introduced in the argument of the cosine signal of the fringes. This change, in digital fringe profilometry, is modeled by software. The phase modulation can be either spatial, temporal or a combination of both, thus these changes are called *spatiotemporal carrier* $c(x, y, t)$. They can be introduced in the mathematical model of the fringes in Eq. (1.1) as follow

$$I(x, y, t) = a(x, y) + b(x, y)cos[\varphi(x, y) + c(x, y, t)]. \qquad (3.1)$$

To be able to isolate the searched phase of the fringes, the carrier $c(x, y, t)$ must have a higher frequency in comparison to the phase $\varphi(x, y)$. That is

$$\|\nabla c(x, y, t)\| > \|\nabla\varphi(x, y)\|_{max}, \qquad (3.2)$$

where ∇ is the nabla operator defined as

$$\nabla = \left(\frac{\partial}{\partial x}, \frac{\partial}{\partial y}\right). \qquad (3.3)$$

The spatiotemporal carrier is a useful tool to detach the analytical signal $1/2\, b \exp[i\varphi(x, y)]$, which solves the phase demodulation process. Also, it solves the phase ambiguity of the cosine signal, since $\cos(\varphi + c) \neq \cos(-\varphi + c)$. Some typical examples of carriers used in digital interferometry are presented below, they are just for demonstrative purposes and without units.

- Linear temporal [16]/spatial carrier with vertical fringes (Fig. 3.2).

$$c_1(x, y, t) = u_0 x + \omega_0 t. \qquad (3.4)$$

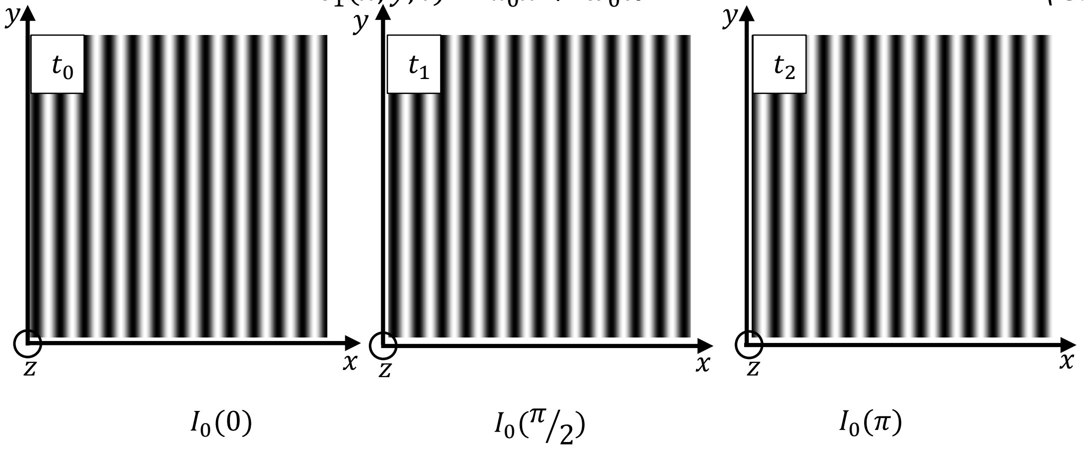

Fig. 3.2.-Linear temporal/spatial carrier with vertical fringes. With $u_0 = {}^{\pi}/_{12}$ *and* $\omega_0 = {}^{\pi}/_{2}$.

- Tilted spatial carrier [17] (Fig. 3.3).

$$c_2(x,y) = u_0 x + v_0 y. \tag{3.5}$$

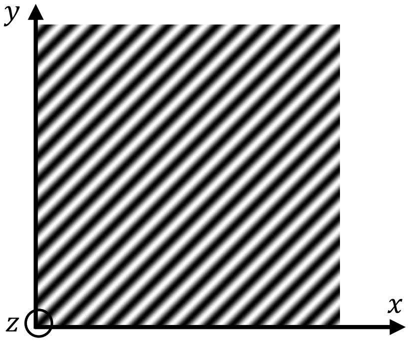

Fig. 3.3.-Tilted spatial carrier with $u_0 = v_0 = {}^{\pi}/_{12}$.

- Conic carrier [18] (Fig. 3.4).

$$c_3(x,y) = \omega_0 \rho; \qquad \rho = \sqrt{x^2 + y^2}. \tag{3.6}$$

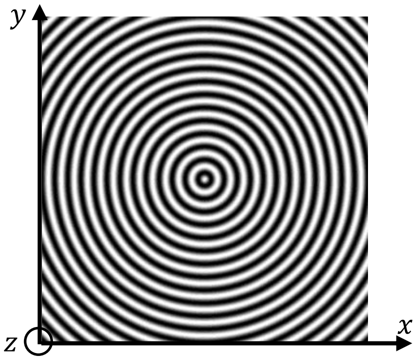

Fig. 3.4.-Conic carrier with $\omega_0 = {}^{\pi}/_{12}$.

- 2 × 2 Pixelated carrier [19] (Fig. 3.5).

$$e^{ic_4(x,y)} = \exp\left[i\omega_0 \begin{pmatrix} 1 & 2 \\ 3 & 4 \end{pmatrix}\right] ** \sum_{m=0}^{\infty} \sum_{n=0}^{\infty} \delta(x - 2m, y - 2n), \tag{3.7}$$

where $\omega_0 = {}^{\pi}/_{2}$, the symbol ** is the operation of convulution in two dimensions and δ is a two-dimensional Dirac delta.

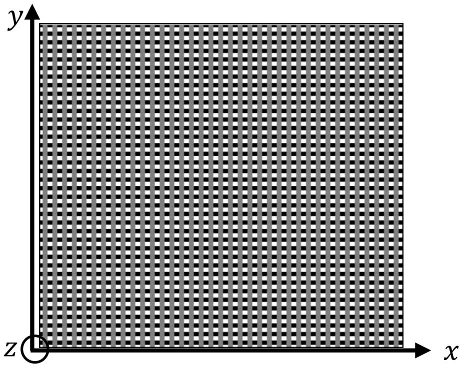

Fig. 3.5.-2x2 pixelated carrier where $\omega_0 = \pi/2$.

- 3×3 pixelated carrier [20, 21] (Fig. 3.6).

$$e^{ic_5(x,y)} = \exp\left[i\omega_0 \begin{pmatrix} 1 & 2 & 3 \\ 8 & 9 & 4 \\ 7 & 6 & 5 \end{pmatrix}\right] ** \sum_{m=0}^{\infty}\sum_{n=0}^{\infty} \delta(x-2m, y-2n), \qquad (3.8)$$

where $\omega_0 = {}^{2\pi}/_{9}$.

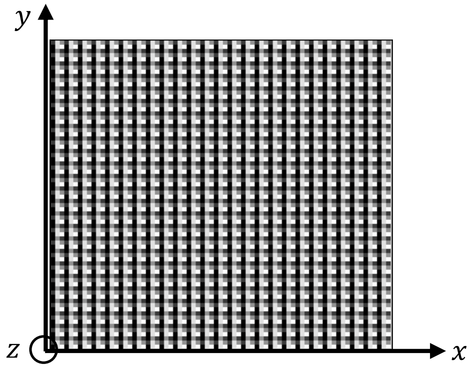

Fig. 3.6.-3x3 pixelated carrier.

The value of ω_0 in the carriers shown above, except with the pixelated ones, was chosen arbitrary and only for illustrative purposes. These carriers allow us to demodulate different kind of interferograms. The type of experiment will determine which carrier will be used. For example, the temporal carrier is useful to demodulate closed fringe interferograms [17], but only in static phenomena where $\varphi(x, y)$ doesn't vary through time during the phase acquisition. To study fast dinamyc events we can use the carrier in Fig. 3.2, but without the time dependency [9, 17], that makes possible demodulate an open fringe pattern with one single image.

The conic carrier (Fig. 3.4) has been used to study the corneal topography and recently, it has been proved that the periodic concentric ring pattern can be phase-demodulated using synchronous interferometric methods [18]. In 2014, *Gonzalez et al.* [22] presented an algorithm that analyzes images captured with a modified Hartmann plate. Like the method described in [18], this method demodulates a signal with a conic-wavefront carrier by using synchronous interferometric techniques.

Padilla et al. [21] proven the efficiency of a 9-step, 3x3 pixelated carrier to phase-demodulate intensity-distorted fringe patterns. It was shown, that the 3x3 pixelated carrier has higher harmonic rejection than the 2x2 pixelated one. Also, the harmonic robustness of this carrier equals the robustness of the temporal least-squares 9-step phase-shifting algorithm.

3.2. Fourier method.

The Fourier transform method (FTM) has been used in fringe analysis since 1972 [17], and then formalized by *Takeda* in 1982 [9]. This is a spatial carrier method that, basically, consists in computing the spectrum of a fringe pattern signal through the Fourier transform, then a low-pass filter is applied to isolate the analytic signal from which the searched phase can be extracted. This method will be explained with a real profilometry experiment developed in the laboratory of digital image processing.

Let's begin with the equation of a digital fringe pattern captured by a CCD camera as follows,

$$I(x,y) = a(x,y) + b(x,y)\cos[\varphi_0(x,y) + c(x,y)], \tag{3.9}$$

where $c(x,y)$ in this case is a linear carrier with vertical fringes, that is

$$c(x,y) = u_0 x. \tag{3.10}$$

From Eq. (3.9), we can separate the cosine function in its exponential components

$$I(x,y) = a(x,y) + \frac{b(x,y)}{2}\left\{e^{i[\varphi_0(x,y)+u_0x]} + e^{-i[\varphi_0(x,y)+u_0x]}\right\}. \tag{3.11}$$

Computing the Fourier transform of the image, with φ_0 constant, we obtain

$$I(u,v) = \mathcal{F}[I(x,y)] = a\delta(u,v) + \frac{b}{2}\left[e^{i\varphi_0}\delta(u-u_0,v) + e^{-i\varphi_0}\delta(u+u_0,v)\right]. \tag{3.12}$$

The above spectrum is composed by three delta signals; the first one $\delta(u,v)$ has amplitude of a and it is centered at the u frequency, the other two delta signals have amplitude of b and phase φ_0, centered at the frequencies $u = u_0$ and $u = -u_0$ respectively. The units of the spatial frequencies u are rad/pixel or rad/mm. Due to the discrete Fourier transform (DFT), the spatial frequencies have discrete values and represent the fringes per field (ff). Therefore, if we have a sampled fringe pattern with *N* points and every sample represents Δx [mm], the relation between the different units is

$$u\left[\frac{\text{rad}}{\text{mm}}\right] \Leftrightarrow \frac{1}{\Delta x}u\left[\frac{\text{rad}}{\text{px}}\right] \Leftrightarrow \frac{\boldsymbol{N}}{2\pi}\frac{1}{\Delta x}\,u[\text{ff}]. \tag{3.13}$$

Returning to Eq. (3.9), one can also shift the frequency of the searched phase to the center of the spectrum, before doing the Fourier transform. This is part of the spatial method developed by Womack [23] in 1984, which is one of the first spatial synchronous methods for linear carrier analysis. In order to center the interest frequency, we need to multiply the Eq. (3.11) by a linear carrier reference given by

$$c(x,y) = \exp[u_0 x]. \tag{3.14}$$

Then, Eq. (3.11) can be rewritten as follow

$$I(x,y) = a(x,y)e^{iu_0x} + \frac{b(x,y)}{2}\left\{e^{i[\varphi_0(x,y)+2u_0x]} + e^{-i[\varphi_0(x,y)]}\right\}. \tag{3.15}$$

For simplicity, let's assign a variable for the term of fringe contrast $b(x,y)$ and the constant phase $\varphi_0(x,y)$:

$$I_\varphi(x,y) = \frac{b(x,y)}{2}e^{-i\varphi_0(x,y)}. \tag{3.16}$$

With this variable change, the Eq. (3.15) can be rewritten as

$$I(x,y) = a(x,y)e^{iu_0x} + I_\varphi^*(x,y)\exp(2iu_0x) + I_\varphi(x,y). \tag{3.17}$$

Now, we can compute the Fourier transform of this new equation, modulated by the linear carrier reference, and get the spectrum of the signal as

$$\mathcal{F}[I(x,y)] = I(u,v) = a\delta(u-u_0,v) + I_\varphi^*(u-2u_0) + I_\varphi(u,v). \tag{3.18}$$

From Eq. (3.18) we can see three terms. Two of them are high-frequency signals; one is a DC and the other one is the lobe I_φ^*, centered at $u = +u_0$ and $u = +2u_0$ respectively. The third term is the low-frequency analytic signal and carries the modulating searched phase. Also, after the modulation the spectrum (Eq. 3.11) is shifted by an amount $\Delta = -u_0$ in the frequency space.

The next step is to separate the lobe I_φ in the modulated spectrum using a low-pass filter. Using $H(u,v)$, that is the FTF of the low-pass filter, the analytic signal will be recovered as

$$I_\varphi(u,v) = H(u,v)\,I(u,v). \tag{3.19}$$

Once the interferogram signal is filtered, we apply the inverse Fourier transform (IFT) to return to the space domain and get the searched complex analytic signal.

Then, we can finally compute the arctangent (angle) of this complex value to get the wrapped phase of the interferogram. This operation is given by

$$\varphi_W = \text{angle}(I_\varphi). \tag{3.20}$$

In order to understand better this method, next is shown a real profilometry experiment made in the laboratory, using the Fourier Transform Method (FTM) to demodulate the interferogram. Fig. 3.7 shows an object (theater mask) with vertical fringes projected.

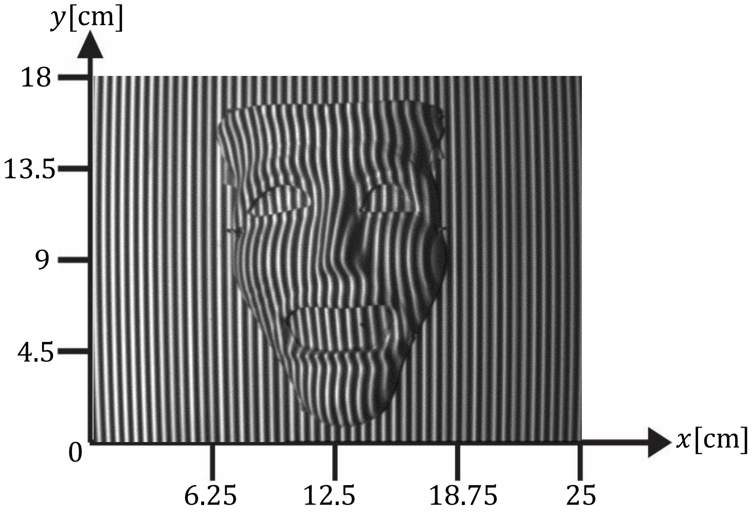

Fig. 3.7.-Image captured of an arbitrary object with vertical fringes projected onto it, with size of 640 x 480 pixels. Physical representation of Eq. (3.9).

As we can see in Fig. 3.7, in order to apply the FTM we need to have an image with a high fringe density, that is, one must project a high-frequency fringe pattern onto the object. The reason of this is shown in the spectrum of this image (Fig. 3.8), where the distance between the frequency lobes will be larger in comparison to an image with low-frequency fringes.

In this example, the spatial frequency was $u_0 x = \frac{2\pi}{12}\Delta x \ [\mathrm{rad/px}]$, that is 12 pixels per fringe.

In Fig. 3.8, the spectrums of the captured image are shown. The first graph, Fig. 3.8 a), is the spectrum of the image before the linear carrier modulation, and in Fig. 3.8 b) shows the spectrum after the modulation, with the low-frequency signal on the origin.

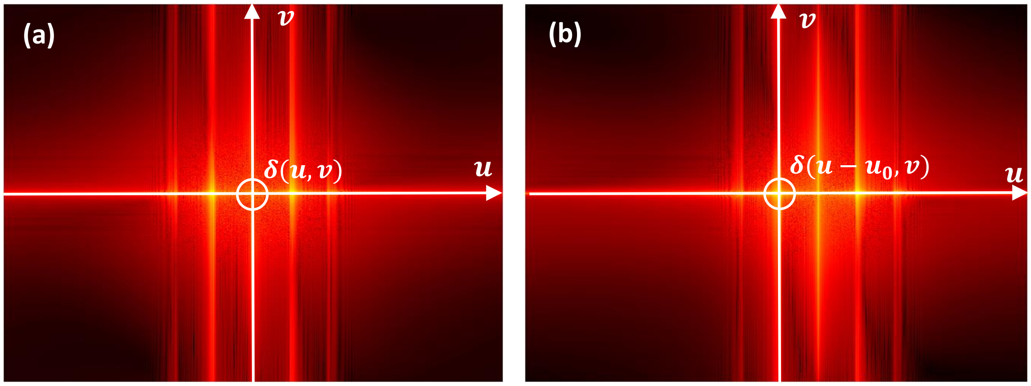

Fig. 3.8.-(a) Spectrum before the linear modulation with the frequency axis v and u. (b) Spectrum after linear modulation.

In the spectrum, we can see some harmonics signal, due to the intrinsic noise of the CCD camera and the projected fringes. We are only interested in the first lobe frequency, so we need to isolate it in order to demodulate the signal.

Fig. 3.9 (a) shows the results of apply the low-pass filter of Eq. (3.19), over the modulated spectrum (Fig. 3.9a). The retrieve wrapped phase of the image, computed from the angle of the analytic signal as in Eq. (3.20), can be seen in Fig. 3.9 (b).

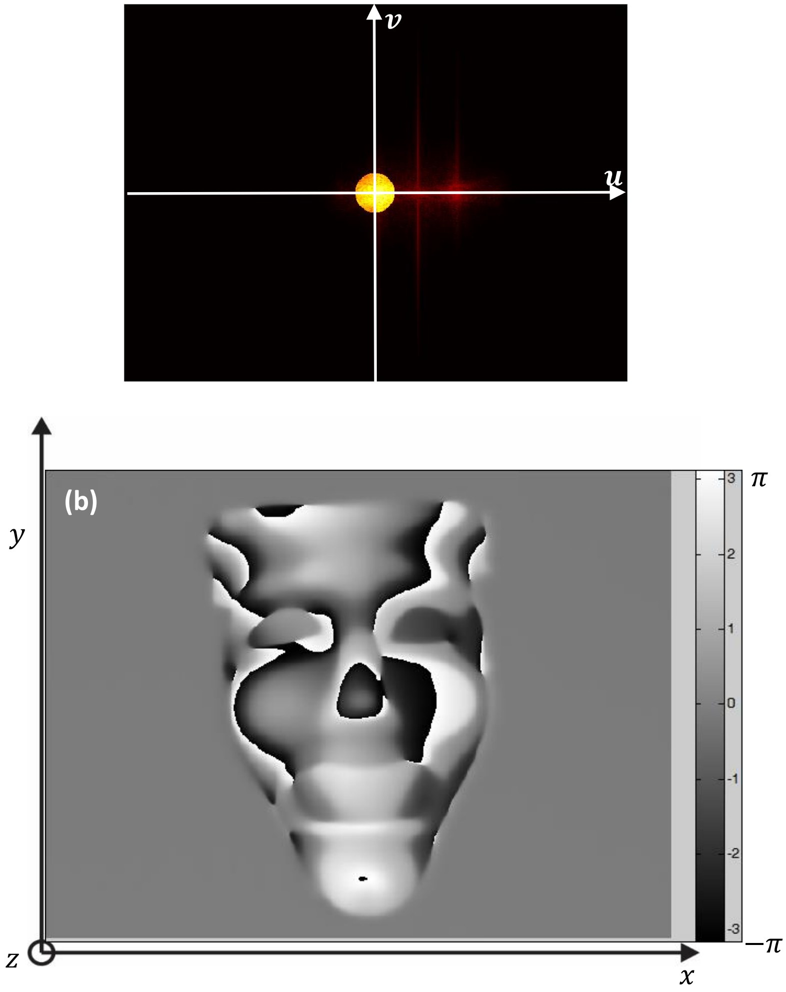

Fig. 3.9.-(a) Spectrum of the image. (b) Recovered phase of the image.

The unwrapped phase in Fig. 3.9 (b) will be shown and widely described in the chapter 4: Phase unwrapping.

3.3. Phase-shifting interferometry (PSI).

The phase-shifting is a temporal method where a sequence of interferograms are recorded while the reference phase is shifted/changed by a constant step. The wavefront phase is encoded in the variations on the intensity pattern of the recorded interferograms, and a simple point by point calculation recovers the phase. This method has its initial reference back to 1966 (*Carré*, 1966) [24], but the beginning of the development of PSI was on the 70's with the work of *Bruning et al. (1974)* [16].

In fringe projection, this method can be done by introducing a uniform phase step between successive images. As seen in chapter one, the several images of the temporal phase-shifted interferogram is given by

$$I(x,y,t) = a(x,y) + b(x,y)\cos[\varphi(x,y) + \omega_0 t], \qquad (3.21)$$

where $\omega_0 t$ represents the temporal-carrier phase modulation.

Now, let's analyze Eq. (3.21) in the frequency domain by computing its Fourier transform to get

$$\begin{aligned} I(x,y,\omega) = a(x,y)\delta(\omega) + \left(1/_2\right)b(x,y)\exp[i\,\varphi(x,y)]\,\delta(\omega-\omega_0) \\ + \left(1/_2\right)b(x,y)\exp[-i\,\varphi(x,y)]\,\delta(\omega+\omega_0). \end{aligned} \qquad (3.22)$$

The equation above can be visualized in Fig. 3.10. As we can see, the high-frequency temporal carrier modulation produces spectral separation between the signals of the interferogram. Which helps to obtain a phase estimation of $\varphi(x,y)$ modulo 2π.

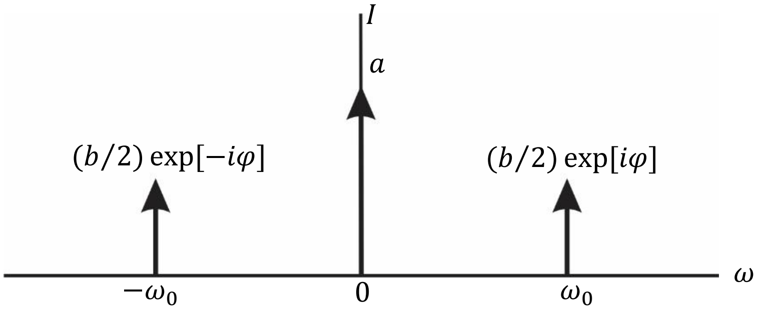

Fig. 3.10.-Spectrum of the temporal carrier phase-modulated fringe pattern.

In a similar way with the Fourier method, we are going to use a real experiment to describe the phase-shifting technique. A basic profilometry technique was used to project fringes with a constant shift in the phase of $\pi/2$ between fringe samples and a spatial frequency of $u_0 = \pi/4$. Fig. 3.11 shows the images captured by a CCD camera with a resolution of 640x480 pixels, using projected fringes over an object with a human face form.

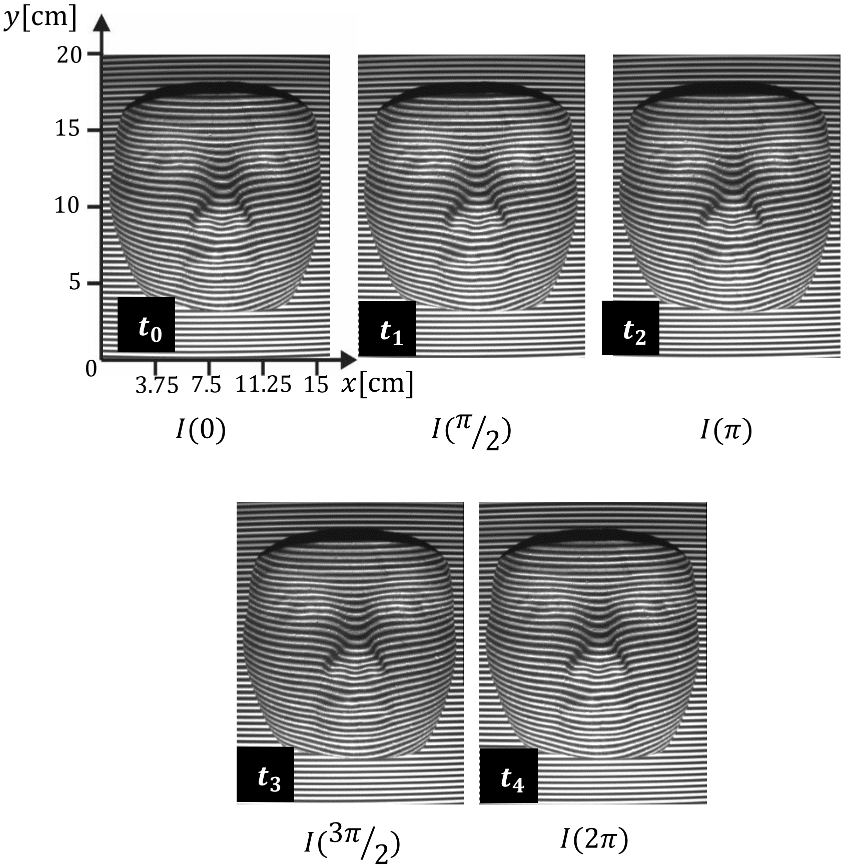

$I(0)$ $I(^{\pi}/_{2})$ $I(\pi)$

$I(^{3\pi}/_{2})$ $I(2\pi)$

Fig. 3.11.-Recorded images with a phase-shifted fringe patternamong them. The fringes were projected with a Dell projector with resolution of 1024 x 768 pixels, numerical aperture of F/2.8. The image sensor was a Sony CCD monochromatic camera XC-ST50 with a resolution of 640 x 480 pixels.

As it is shown, five images were taken for the same object, but introducing a temporal carrier in the fringe pattern projected. In the next sections of Phase-Shifting algorithms (PSA's), will be described and implemented an algorithm to demodulate these fringes in order to retrieve the optical phase (where the form is encoded) of the object.

3.3.1. Linear Phase-Shifting Algorithms (PSAs).

A phase-shifting algorithm can be described as a quadrature linear filter and it is characterized by its impulse response function $h(t)$, or by its FTF in the Fourier domain [6], $H(\omega)$:

$$h(t) = \sum_{n=0}^{N-1} c_n \delta(t-n) \tag{3.23}$$

$$\mathcal{F}[h(t)] = H(\omega) = \sum_{n=0}^{N-1} c_n \exp(-i\omega n) \tag{3.24}$$

If the FTF fulfills the quadrature conditions given by

$$H(0) = H(-\omega_0) = 0, \quad H(\omega_0) \neq 0, \tag{3.25}$$

then, $h(t)$ is a valid quadrature linear filter for an interferometric signal like Eq. (3.21). Therefore, applying this quadrature filter we get the following analytic signal:

$$I(t) * h(t) = \sum_{n=0}^{N-1} c_n I(x,y,n) = A_0(x,y) \exp[i\varphi_W(x,y)]. \tag{3.26}$$

Now, from the Eq. (3.26) and computing its angle, the wrapped phase $\varphi_W(x,y)$ can be obtained. The amplitude $A_0(x,y) \in \mathbb{C}$ contains information about the local contrast of the quadrature linear filter:

$$A_0(x,y) = (1/2)\, b(x,y)\, |H(\omega_0)| \exp\{i\, angle[H(\omega_0)]\} \tag{3.27}$$

It may happens that the temporal samples of the interferogram and the quadrature linear filter are not tuned at the same frequency ω_0. This is called *detuning error* $D(\Delta)$, and occurs when the actual sampling frequency is $\omega_0 + \Delta$. Thus, the resulting phase estimation is given by

$$\hat{\varphi}(x,y) = \varphi(x,y) - D(\Delta) \sin[2\varphi(x,y)], \tag{3.28}$$

where $D(\Delta)$ is calculated by the following ratio

$$D(\Delta) = \frac{|H(-\omega_0 - \Delta)|}{|H(\omega_0 + \Delta)|}, \tag{3.29}$$

for $|\Delta/\omega_0| \ll 1$. It can be infered from the above equation, that the detuning error causes a distortion in the estimated phase of twice the original fringe frequency. Furthermore, in real life experiments the signals are distorted by some amount of noise. Therefore, it is important to know the signal-to-noise power ratio of a PSA, which is given by

$$G_{\frac{S}{N}}(\omega_0) = \frac{|H(\omega_0)|^2}{(1/2\pi) \int_{-\pi}^{\pi} |H(\omega_0)|^2 \, d\omega}. \tag{3.30}$$

Also, the objective of the linear quadrature filter is to isolate the signal $(b_1/2) H(\omega_0) \exp(i\omega)$, so we need to consider the harmonic rejection capabilities of the PSA. This means to generalize the quadrature conditions to

$$\begin{aligned} &H(\omega_0) \neq 0, \\ &H(-\omega_0) = 0, H(0) = 0, \\ &H(-n\omega_0) = 0, H(n\omega_0) = 0. \end{aligned} \tag{3.31}$$

Analyzing these conditions, we can assume that the searched phase is at the frequency ω_0, and all the others frequencies multiples of ω_0 must be equal to zero.

To complete the analysis, the FTF can be numerically evaluated by plotting $|H(\omega_0)|$ versus (ω/ω_0) and see if the FTF has null response at the normalized frequencies $(\omega/\omega_0) = \{\pm 2, \pm 3, \pm 4\}$.

3.3.2. Least-squares phase-shifting algorithm (LS-PSA)

Bruning proved in 1974 [16], that the phase-extraction algorithms in phase-measurement interferometry can be developed from the principle of the least square estimation. Later in 1982, Morgan [25] developed an algorithm that extracts the phase in the presence of a linear time-dependent drift, proving the advantages of using LS-PSAs for phase estimation in temporal interferometry.

In the arctangent formulation, a general *N-step* LS-PSA equation is given by

$$\tan[\hat{\varphi}(x,y)] = \frac{\sum_{n=0}^{N-1} \sin(\omega_0 n) I_n}{\sum_{n=0}^{N-1} \cos(\omega_0 n) I_n}, \quad \omega_0 = 2\pi/N, \tag{3.32}$$

where due to the minimum 3 steps condition in PSAs; $N \geq 3$. If we rewrite Eq. (3.32) using the FTF formalism, we get

$$A_0 \exp[i\, \hat{\varphi}(x,y)] = \sum_{n=0}^{N-1} \exp(i\omega_0 n)\, I(n) = I(t) * \sum_{n=0}^{N-1} \exp(i\omega_0 t)\delta(t-n) \tag{3.33}$$

where $A_0 = (b/2)H(\omega_0)$ is the amplitude of the filtered signal. Therefore, the impulse response function for the N-step LS-PSA is described by

$$h(t) = \sum_{n=0}^{N-1} \exp(i\omega_0 t)\delta(t-n), \tag{3.34}$$

and its FT is given by

$$H(\omega) = \sum_{n=0}^{N-1} \exp[in(\omega - \omega_0)]. \tag{3.35}$$

According to Surrel [26] the FTF of the N-step LS-PSAs can also be written as

$$H(\omega) = \prod_{n=0}^{N-2} [1 - \exp i(\omega + \omega_0)]. \tag{3.36}$$

Getting back to the example of the images taken to explain the phase-shifting technique (Fig. 3.11), we are going to use a 5-step LS-PSA to retrieve the phase of these images. We will set $\omega_0 = 2\pi/5$, due to the number of steps taken. This PSA will be described to understand its performance. So, for our example of 5-step LS-PSA the FTF is described by

$$H(\omega) = \prod_{n=0}^{3} [1 - \exp i(\omega + \omega_0)]. \tag{3.37}$$

To analyze this 5-step algorithm we can first plot its FTF using just the magnitude of this function ($|H(\omega)|$), the obtained graph is shown in Fig. 3.12.

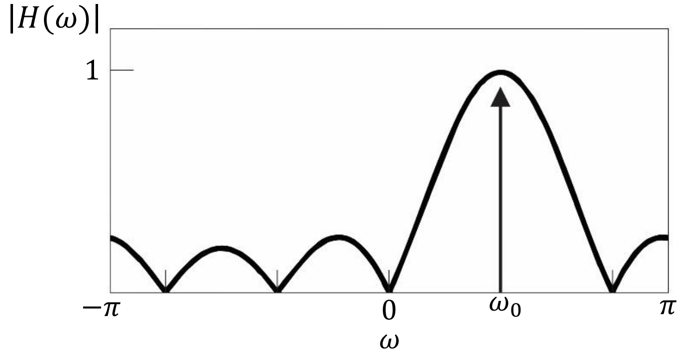

Fig. 3.12.-Frequency transfer function $|H(\omega)|$.

According to this figure, the maximum of the filter is at the interest frequency ω_0. Also, it can be seen that the first-order zeros are at $\{0, -\omega_0, \pm 2\omega_0\}$, therefore this PSA does not possess robustness against detuning errors.

We can extend the plot of $|H(\omega)|$ with the normalized-frequency (ω/ω_0), in the range of $-4\pi \geq (\omega/\omega_0) \geq 4\pi$ for example, to see its harmonic response. This can be seen in Fig. 3.13.

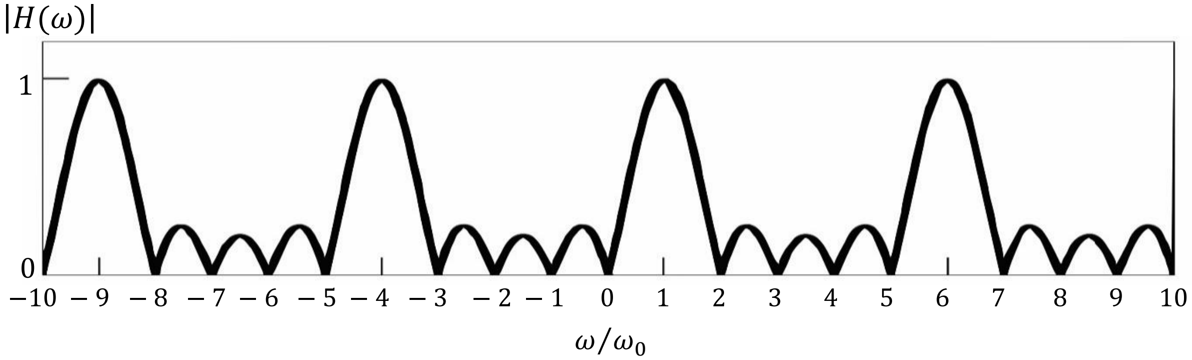

Fig. 3.13.-Normalized-frequency harmonics response.

From that plot we can see the harmonics that won't be rejected by the 5-steps LS-PSA. Again, we are only interested in the frequency ω_0, marked in the plot as 1.

Now to retrieve the phase of this example, is necessary to implement the analytic formulation of this PSA is given by

$$A_0(x,y)\exp[i\varphi_W(x,y)] = \sum_{n=0}^{4} \exp(i\omega_0 n). \tag{3.38}$$

With the equation (3.38) the amplitude can be retrieved of the interferogram images and its phase. In order to get the searched phase we can compute the angle of Eq. 3.37. The Fig. 3.14 shows the recovered wrapped phase resulting of the implementation of this algorithm.

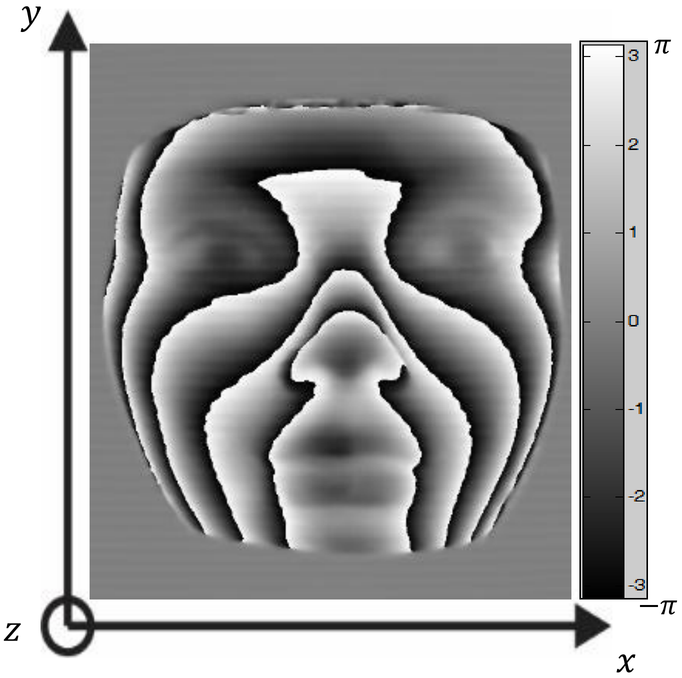

Fig. 3.14.-Retrieved wrapped phase of the sequence of 5 samples for phase-shifting technique.

Finally, to reconstruct the form of the object we can do an unwrapping-phase processing. The theory and algorithms to unwrap the phase of an interferogram will be discuss in the following chapter.

4. Phase unwrapping.

In the previous chapter were discussed two techniques to determine the phase term in an interferogram. Now, the final step is to convert this wrapped phase (discontinuous phase) into a continuous phase map. This process is known as phase unwrapping, and it is defined as the process by which the absolute value of a phase angle that extends over a range of more than 2π is recovered [27]. In this chapter is described the theory of some phase unwrapping methods and their implementation.

4.1. The phase unwrapping problem.

Usually, phase estimation methods in fringe analysis conclude with an expression of the form

$$\varphi = \arctan\left(\frac{a}{b}\right), \tag{4.1}$$

where a and b are functions of the gray levels within the original fringe pattern, and φ is the phase value within a single fringe. As seen in chapter 3, the nature of the terms a and b will depend on the fringe analysis technique implemented. For example, in the Fourier method the terms will be the imaginary and real parts of the complex result from the inverse Fourier transform of the filtered spectrum, whereas if the phase-shifting method was applied the terms will be a series of intensity values taken from the same pixel location in the samples.

The arctangent function is bound within the values of $\pm\pi$. This means that there are discontinuities bounded the sides of the fringe. So, the unwrapping is done by looking for the $0 \leftrightarrow 2\pi$ jumps in the wrapped phase map, where the basic criterion is

$$\begin{gathered} \varphi(x_{n+1}, y_n) - \varphi(x_n, y_n) < -\pi \Rightarrow \text{add } 2\pi \text{ to } \varphi(x_{n+1}, y_n); \text{increment } k. \\ \varphi(x_{n+1}, y_n) - \varphi(x_n, y_n) > \pi \Rightarrow \text{subtrac } 2\pi \text{ from } \varphi(x_{n+1}, y_n); \text{decrement } k. \end{gathered} \tag{4.2}$$

This means that, phase jumps of more than half a fringe are forbidden and are taken to indicate that the next-order fringe begins. Therefore, the phase unwrapping problem may be formally stated as: given a discontinuous phase $\varphi_W(x,y) \in [-\pi,\pi]$, find the continuos phase $\hat{\varphi}(x,y) \in \mathbb{R}\,[0,2\pi]$ such that

$$W[\hat{\varphi}(x,y)] = \varphi_W(x,y). \tag{4.3}$$

W is the wrapped operator, and is defined as follow

$$W[x] = \arctan\left\{\frac{\sin(x)}{\cos(x)}\right\}, \tag{4.4}$$

where $W\colon \mathbb{R}^1 \rightarrow (-\pi,\pi)$.

4.2. Quality-guided flood-fill phase unwrapping.

To avoid a wrong unwrap phase computation one can do some treatment to the wrap phase field before the unwrapping process starts. Recently, it have been used phase methods based on get quality maps of the wrap phase estimation [29, 30], and also adding a scanning pixel paths using a flood-fill algorithm [31]. In this section, the used method is described to get the continuous phase map of some of the objects measured during this project. The algorithm of this method consists of three steps. It begins masking out the invalid data phase in the pixels, this means, pixels with shadows or pixels outside the contour of the object. Then, a quality phase map is generated depending on the magnitude of each pixel dividing the phase map into several areas. Finally, a flood-fill algorithm is implemented to scan and unwrap the pixels in each quality area.

Firstly an algorithm was implemented to mask out the shadows of the phase map and the object contour, that means, the areas where the phase is not well defined or is outside the boundary of the object. So, the algorithm will recognize this areas as invalid zones, and it won't try to unwrap them, avoiding the error propagation through the adjacent pixels. In order to detect the invalid phase pixels, we use the magnitud of the complex function, which was retrieved by some of the demodulation methods of an interferogram. Depending of the magnitude data of this function, a threshold value was chosen to decide if the current pixel analized has an invalid phase value. The resulting pixels with invalid phases were labeled with a Not-a-Number (NaN) value, the valid ones were labeled with a '1'. The criterion of this pixel classification is shown in the following equation

$$\text{Mask} = \begin{cases} 1 & \text{if } |A_0 \exp[i\varphi_W]| \geq \text{ threshold} \\ \text{NaN} & \text{if } |A_0 \exp[i\varphi_W]| < \text{ threshold} \end{cases} \tag{4.10}$$

This process will be explained with an example. The complex function $A_0 \exp[i\varphi_W]$ was retrieved using the phase shifting technique over an object. Fig. 4.4 (a) shows the extracted phase of this object, this means, the angle of the complex function. In the Fig. 4.4 (b) we can see the same wraped phase but after an average 3x3 convolution filter is applied. Meanwhile, Fig. 4.4 (c) shows the magnitude of the complex function of the interferogram.

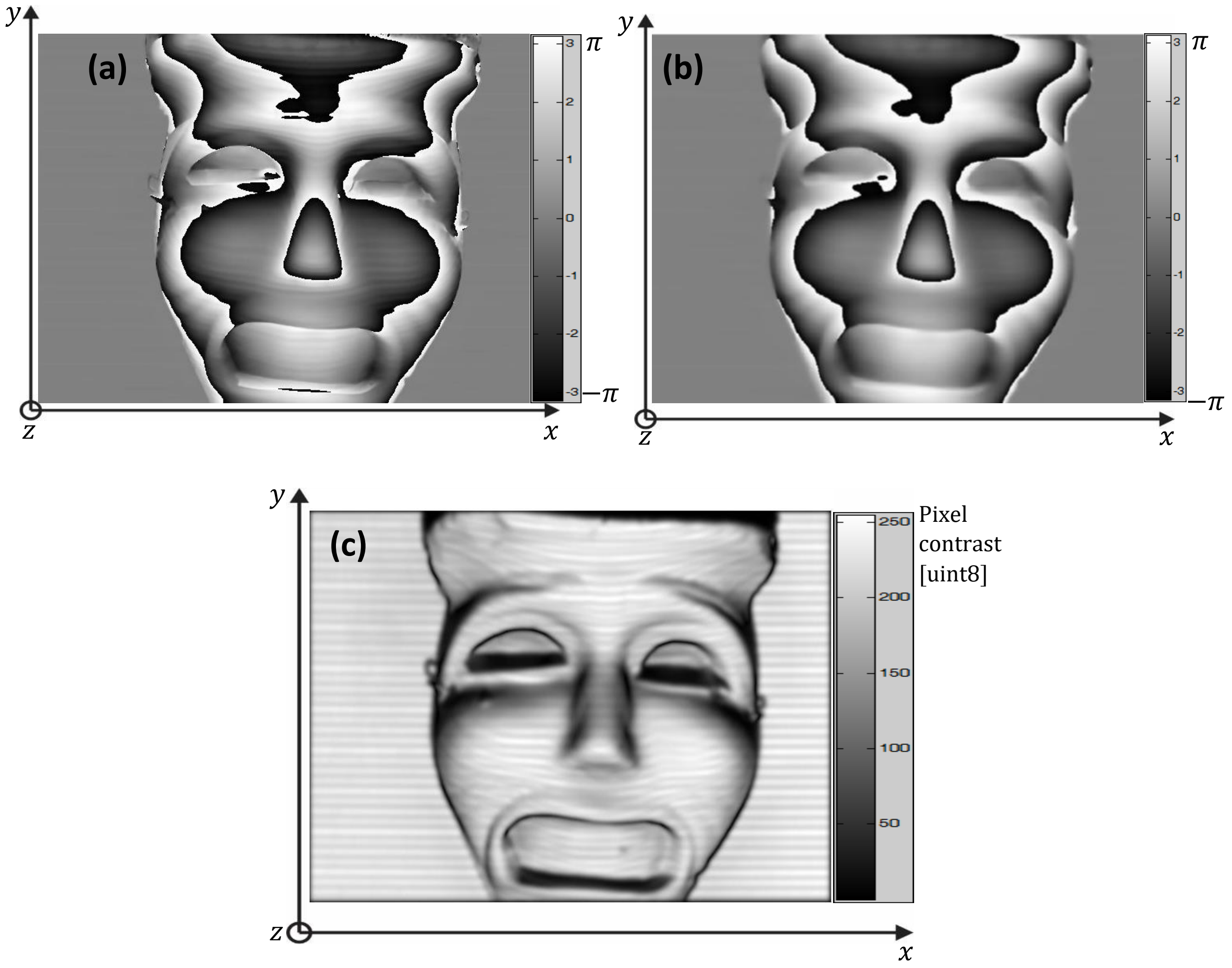

Fig. 4.4.-Wrapped phase of an object: (a) Unfiltered wrapped phase. (b) Filtered wrapped phase. (c) Magnitude of the interferogram object with the same size of images in a and b.

Using the magnitude map visualized in the figure above, we can construct a mask of the pixels with invalid phase. It is evident that in the black zones the phase is not defined. The fig. 4.5 shows the mask generated with a threshold of $1/30$ (85 in gray level) of the maximum amplitude of the captured image.

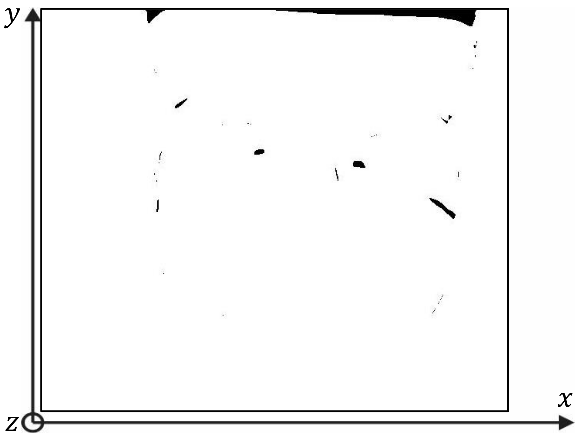

Fig. 4.5.-Mask of the interferogram with the invalid pixels in black.

When the amplitude decay at lower than $(1/30)\ \mathrm{abs}(A_0 \exp(i\hat{\varphi}))$ the correspondent pixel is labeled with NaN (colored in black at the figure above), meaning that it is an invalid pixel to unwrap.

The next action, performed by the algorithm, is to identify the different phase quality areas in the image from its correspondent amplitude. The area with the best quality also has the larger amplitude, and doesn't have abrupt discontinuities on the phase. So, the image was divided, and labeled, in 4 different areas according to its amplitude as follow

$$\text{max\_amplitude} = \text{maximun\_value}(|A_0 \exp[i\varphi_W]|) \tag{4.11}$$

$$\text{Area 1} = \left\{\ 1 \quad \text{if } \left({}^{3}\!/_{4}\right)|A_0 \exp[i\varphi_W]| \ \geq |A_0 \exp[i\varphi_W]| \leq \text{max\_amplitude}\right.$$

$$\text{Area 2} = \left\{\ 2 \quad \text{if } \left({}^{2}\!/_{4}\right)|A_0 \exp[i\varphi_W]| \ \geq |A_0 \exp[i\varphi_W]| \leq \left({}^{3}\!/_{4}\right)|A_0 \exp[i\varphi_W]|\right.$$

$$\text{Area 3} = \left\{\ 3 \quad \text{if } \left({}^{1}\!/_{4}\right)|A_0 \exp[i\varphi_W]| \ \geq |A_0 \exp[i\varphi_W]| < \left({}^{2}\!/_{4}\right)|A_0 \exp[i\varphi_W]|\right.$$

$$\text{Area 4} = \left\{\ 4 \quad \text{if Threshold } \geq |A_0 \exp[i\varphi_W]| < \left({}^{1}\!/_{4}\right)|A_0 \exp[i\varphi_W]|.\right.$$

The different quality areas of fig. 4.4 (b), according to the relations in Eq. (4.11), can be seen in Fig. 4.6.

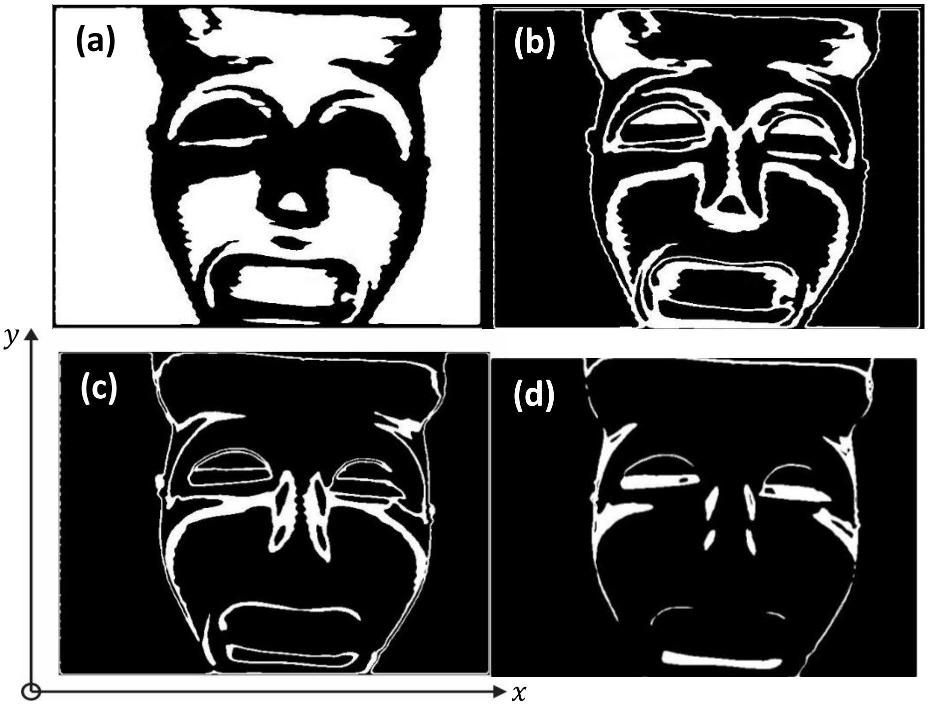

Fig. 4.6.-Different areas according of the quality of the wrapped phase. (a) Area 1, (b) Area 2, (c) Area 3 and (d) Area 4.

The white color on the images means that is a valid pixel for the current area, and therefore its phase can be unwrapped. The unwrap process begins in the best quality area, in order to start with a correct phase estimation of the following areas, until reaching the lower quality phase area. So, the algorithm begins unwrapping a pixel in area 1, and then it checks its surrounding pixels searching for the best quality area (labeled as 1), and so on until reach the low quality pixels.

The scanning is done by the *flood-fill* method. In this method, first is to create an empty queue (Q_1), containing all the pixels to unwrap, checking that the first value is a pixel corresponding to the area 1 of the quality map. Then, the first pixel that pop-up from Q_1 is unwrapped. Once unwrapped, the pixel is labeled as "unwrapped" and it is pushed-out of Q_1. The next step of the algorithm is to check its surroundings searching for the pixel with best quality. Because of the labeled quality areas, the algorithm first searches for a pixel labeled with a '1', if it can't find any the algorithm now search for a '2', and so on until it search for a '4'. This process is repeated until the queue is empty and all the valid pixels are labeled as "unwrapped". The following block diagram (Fig. 4.7) shows the pseudo code of the quality-guided flood-fill unwraping algorithm implemented.

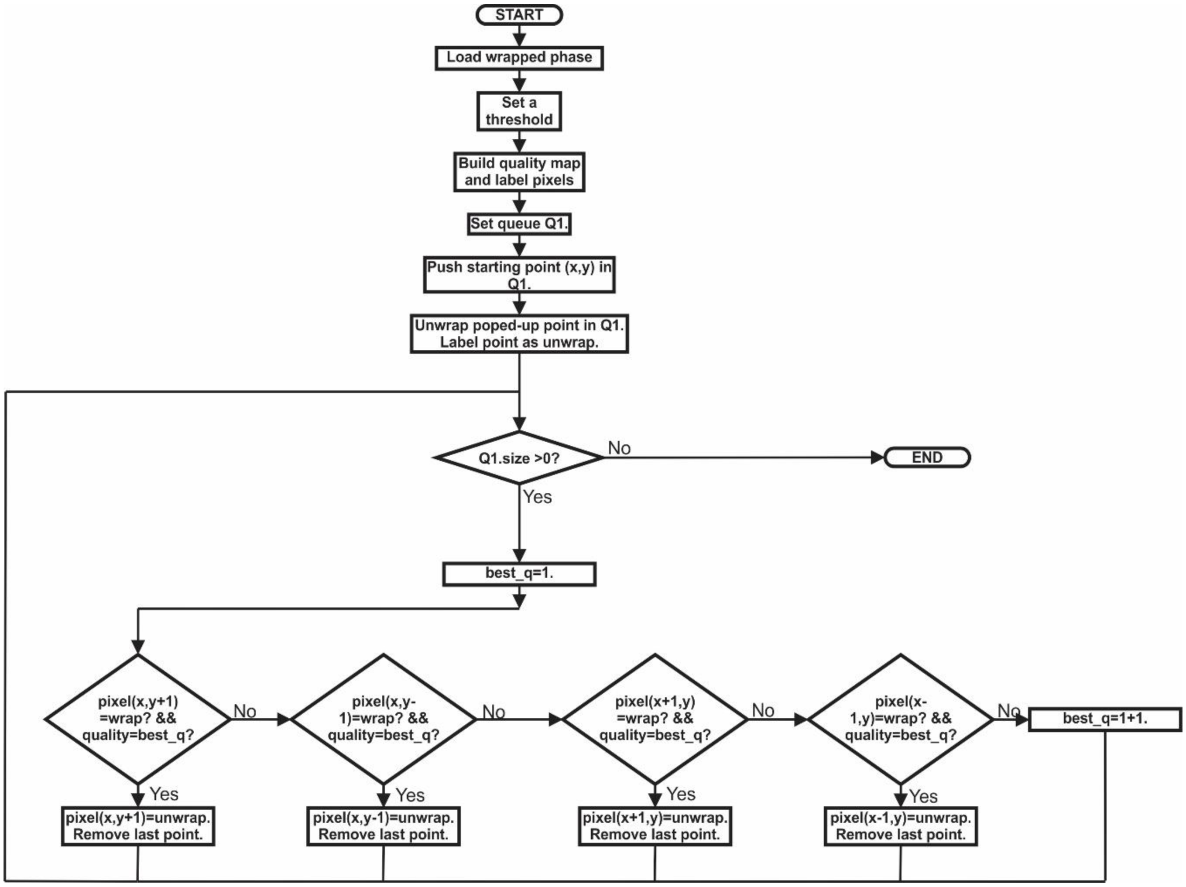

Fig. 4.7.-Block diagram of the quality-guided flood-fill unwrapping algorithm.

This algorithm was implemented in Matlab, however it was necesary to use some java instructions, due to matlab doesn't have instructions to handle queues. Because of that, this algorithm is slow to unwrap relatively large images with size larger than 640x480 pixels.

Fig. 4.8 shows the unwrapped phase using the algorithm with the method here explained. The wrapped phase corresponds to the one of the Fig. 4.4 (b).

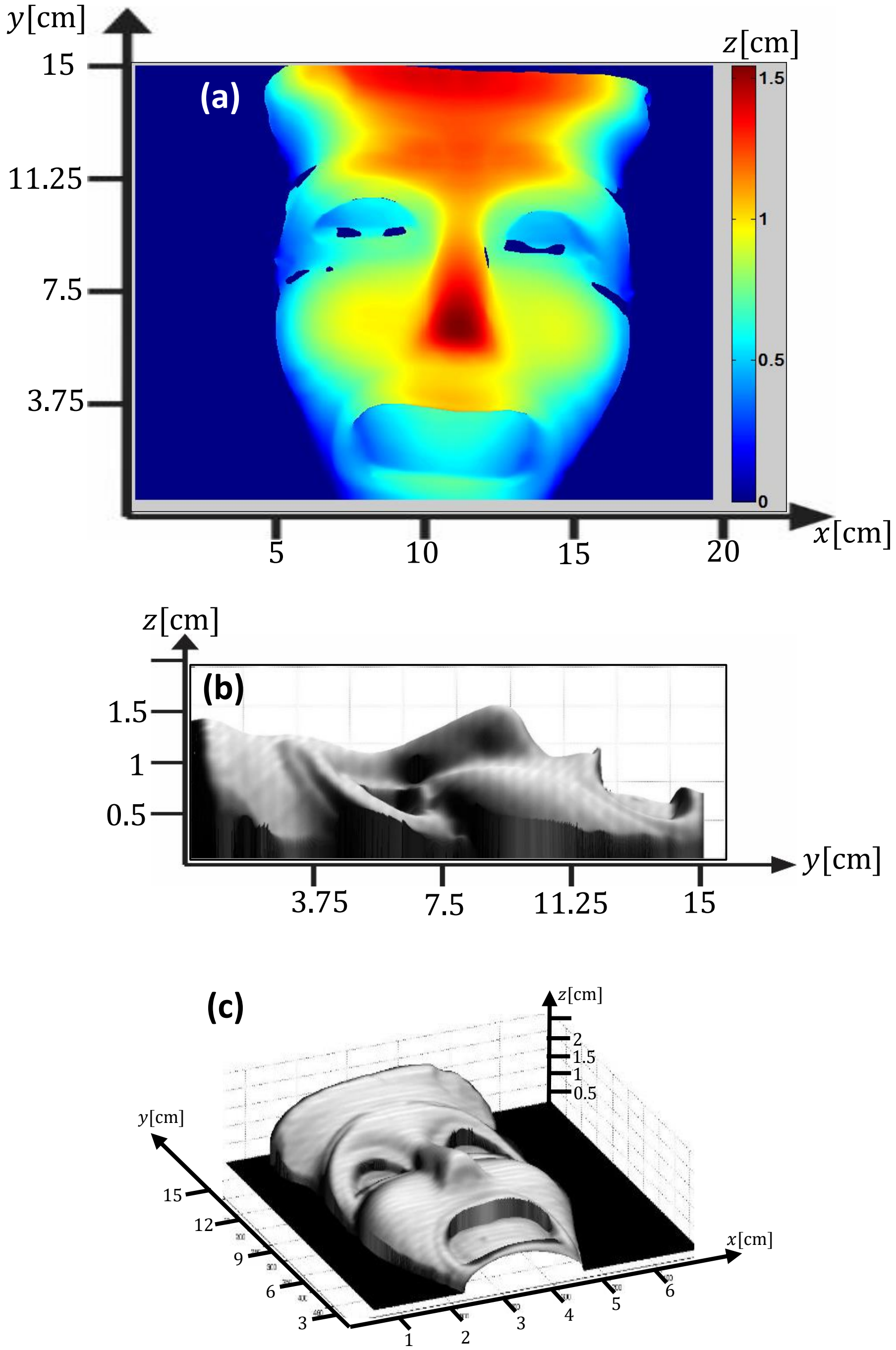

Fig. 4.8.-Unwrapped phase of the object. (a) Unwrapped phase, (b) Transversal view of the reconstructed object. (c) Depth view of the reconstructed object.

The black pixels that can be seen in Fig. 4.8 (a) are due to the mask generated by the algorithm. So, this zones do not have a phase value that can be represented in the graphs.

5. Fringe projection profilometry techniques.

This chapter discusses some fringe projection profilometry techniques implemented to digitalize opaque solids. Three main techniques were performed in this project: co-phase fringe projection, on-axis fringe projection and shape measurement by line projection. Here is presented the description of the set-up used for every technique, as well as the experimental results for each one.

5.1. Co-phase fringe projection profilometry.

The co-phase profilometry setup [32], developed by *Servin et al.,* consists in two projections and one camera with normal vision to the object. The use of two projections has the advantages, regarding to the basic profilometry configuration of one camera and one projector, of solving the self-occluding shadows due to discontinuities. This is achieved by compensating the shadows in one side with the illumination of the opposite projector. Also, it is possible to eliminate the specular reflections generated by the object under study, the same way as with shadows, compensating the illumination of both sides. So, with the coherent combination of different measurements, we can cope the problems of basic fringe projection profilometry techniques. Although this technique can be extended to measure 360-degrees profiles of an object [33], this experiment was performed on a single object's face.

Here were used two projectors Dell s320, with a display resolution of 1024 x 768 pixels (XGA). The image sensor was a Sony CCD monochromatic camera XC-ST50, with a resolution of 640 x 480 pixels, pixel dimension of 8.4 x 9.8 µm, and analog video output with a BNC connector. To digitize the analog video signal and processing this data in the computer, an acquisition digitizer card matrox meteor II was used.

The camera axis was fixed normal respect to the object's surface. The two projectors were placed with opposite angles φ_0 respect to this. The set-up can be visualized in Fig. 5.1.

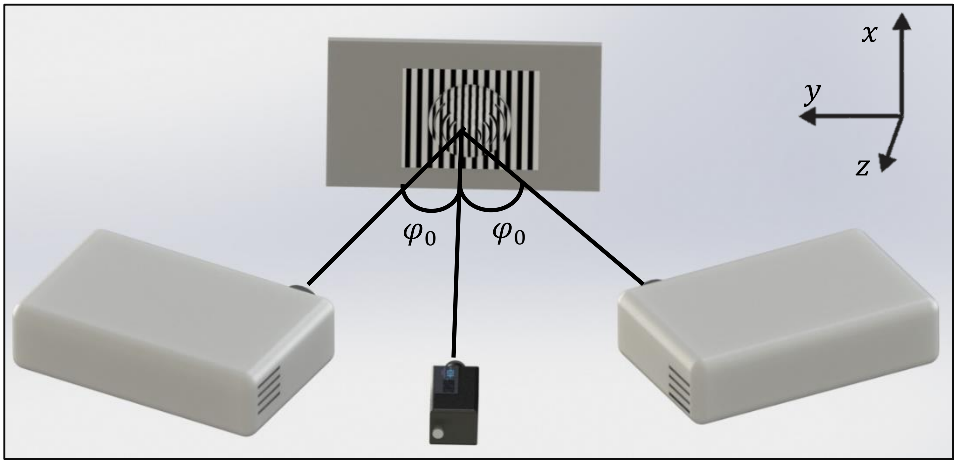

Fig. 5.1.-Co-phase profilometry set-up.

To understand the co-phase profilometry, here is reviewed the mathematical model of it using two projectors and the phase-shifting method. The obtained experimental data consist of two-projection-steps, one for the left projector and another for the right projector. The projected fringes as seen on the CCD camera are given by

$$\begin{gathered} I_L(x,y,\alpha) = a_L(x,y) + b_L(x,y)\cos[\omega_0 x - g\, z(x,y) + \alpha]\,; \\ I_R(x,y,\alpha) = a_R(x,y) + b_R(x,y)\cos[\omega_0 x + g\, z(x,y) + \alpha]\,; \\ \text{with}\ \ \omega_0 = v_0\cos(\varphi_0), g = \tan(\varphi_0) \end{gathered} \tag{5.1}$$

The scanned object is defined as $z(x,y)$. v_0 is the spatial-carrier of the projected fringes. The fringe projection has a phase-sensitivity angle φ_0 respect with the (x,y) plane. The angle α is the shift used in a phase-shifting algorithm (PSA) to demodulate $gz(x,y)$. A four-step least-square phase-shifting algorithm (LS-PSA), with $\alpha = \pi/2$, was implemented in this experiment.

Let's characterize the four-step least-square PSA by analyzing its detuning robustness, signal-to-noise power ratio and its harmonic rejection capabilities. The frequency transfer function (FTF) and its analytic formulation are given by

$$\begin{gathered} H(\omega) = \prod_{n=0}^{2}[1 - \exp i(\omega + \omega_0 n)], \\ A_0(x,y)\exp[i\varphi_W(x,y)] = \sum_{n=0}^{3}\exp(i\omega_0 n), \end{gathered} \tag{5.2}$$

where, as discussed in the previous sections, $A_0(x,y)$ is the amplitude of the retrieve analytic signal, $\varphi_W(x,y)$ is the estimated wrapped phase and $\omega_0 = 2\pi/4$. As seen in chapter 3, to compute its detuning robustness $D(\Delta)$, we can plot the magnitude of its frequency transfer function ($|H(\omega)|$). This plot is shown in Fig. 5.2.

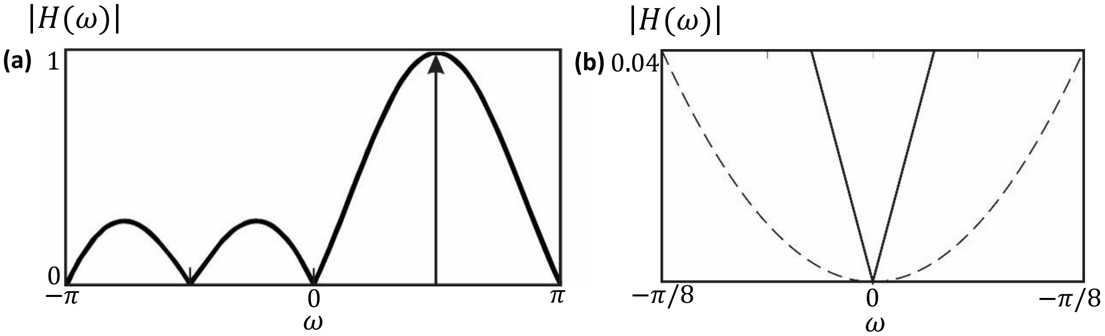

Fig. 5.2.-(a) Frequency transfer function $|H(\omega)|$. *(b) Detuning robustness* $D(\Delta)$.

In these graphs is observed that this algorithm doesn't have a good detuning robustness. This is due that it has first order zeros at $\{0, -\omega_0, \pm 2\omega_0\}$. But, for the experimental purpose this doesn't have a great effect, since this experiment is on static conditions and the phase-step is executed by a controlled software. So, the steps for the phase-shifting are precise and the algorithm does not needs to be robust.

Now, let's analyze the harmonic rejection of the four-step PSA. For this task, we need to plot the FTF versus the normalized frequency ω/ω_0. Fig. 5.3 shows the harmonics response of the used PSA for the co-phase technique.

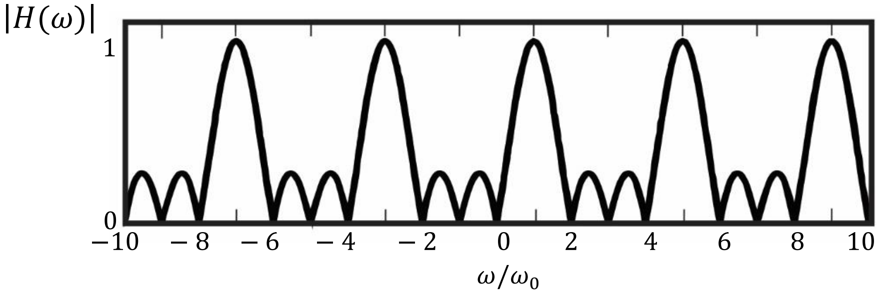

Fig. 5.3.-Normalized-frequency harmonics response for the four-step PSA.

Seeing the previous figure, it is evident that this LS-PSA fails to reject the distorting harmonics {-7, -3, 5, 9} and so on. It has the best harmonic rejection capabilities among the four-step PSA. In fringe projection, one can minimize the harmonics having a good contrast in the fringes and avoiding saturation of the CCD camera.

Finally, to measure the relation between the output signal of this PSA and the level of background noise, we can compute its signal-to-noise power ratio gain. This characteristic is given by the following expression

$$G_{S/N} = \frac{|H(\omega_0)|^2}{(1/2\pi)\int_{-\pi}^{\pi}|H(\omega)|^2 d\omega} = 4 \tag{5.3}$$

Once characterized this PSA, we can apply it to the images captured by the CCD for both side of illumination; one for the left projector and another one for the right projector.

The left projector, gives the following analytic signal for the 4 step PSA

$$A_L(x,y)e^{igz(x,y)} = I_L(0) + I_L\left({}^{\pi}/_{2}\right) e^{i\pi/2} + I_L(\pi)\, e^{i\pi} + I_L\left({}^{3\pi}/_{2}\right) e^{i3\pi/2} \tag{5.4}$$

While the right projector gives:

$$A_R(x,y)e^{-igz(x,y)} = I_R(0) + I_R\left({}^{\pi}/_{2}\right) e^{i\pi/2} + I_R(\pi)\, e^{i\pi} + I_R\left({}^{3\pi}/_{2}\right) e^{i3\pi/2}. \tag{5.5}$$

In the regions where the 3D-object generates self-occluding shadows, the phase $gz(x,y)$ is not defined. But their co-phased sum is perfectly defined all over the phase map

$$\begin{aligned} A(x,y)e^{ikz(x,y)} &= A_L(x,y)e^{igz(x,y)} + \left[A_R(x,y)e^{-igz(x,y)}\right]^*, \\ A(x,y)e^{ikz(x,y)} &= \left[A_L(x,y) + A_R(x,y)\,\right]e^{igz(x,y)}. \end{aligned} \tag{5.6}$$

Now, we can analyze some experimental results obtained with this technique. The object under study was an extruded polystyrene half-sphere (Fig. 5.4), with an irregular fracture to show the shadow effect due to the projector's illumination.

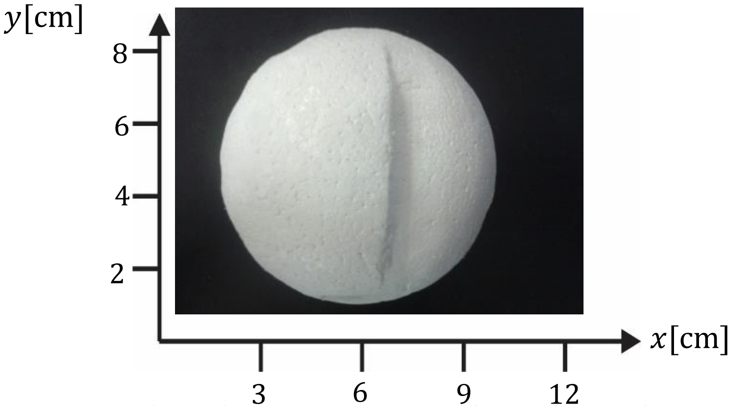

Fig. 5.4.-Object chosen to demonstrate the co-phase technique.

The object was illumined with structured light, in this case were cosinuidal vertical fringes. In order to apply a four-step phase-shifting algorithm, it was necessary to capture 4 images, with a phase shift of $\pi/2$ among them for each projector. Fig. 5.5 (a-d) shows the four phase-shifted fringe patterns with the right projector and the fringe patterns with the left projector are shown in Fig. 5.5 (e-h).

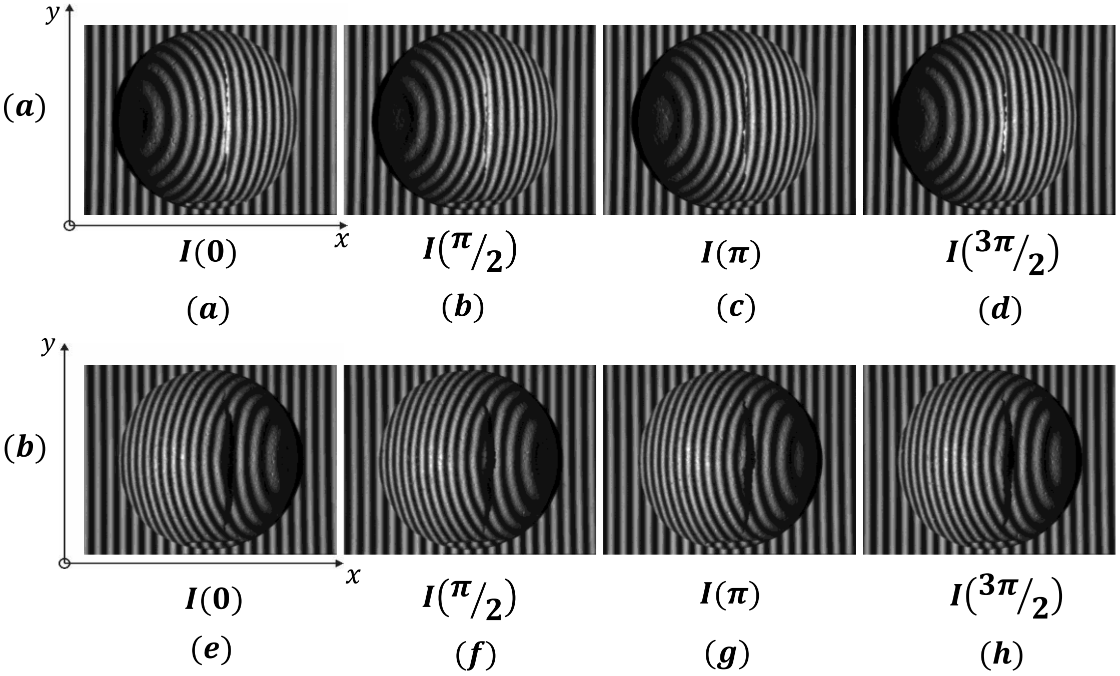

Fig. 5.5.-(a-d) Set of four phase-shifted fringe patterns $\{I(0), I(\pi/2), I(\pi), I(3\pi/2)\}$, as viewed by the CCD camera from the right projector, and (e-h) from the left projector (b).

It is evident the creation of self-occluding shadows on the opposite side of the illumination for each projector. Also, the brightness is different for each illumination, thus the dominant irradiance depends on the incident direction of the light.

Once the pictures in Fig. 5.5 were loaded in the computer, a least squares PSA (Eq. (5.2) and Eq. (5.3)), was implemented to demodulate the fringe patterns. As illustrative purposes, we recover the wrapped phase, obtained with the PSA, with the arctangent function as follow

$$\begin{aligned} \varphi_{LW}(x,y) &= \text{arct}\left\{Im\left[A_L(x,y)e^{igz(x,y)}\right]/Re\left[A_L(x,y)e^{igz(x,y)}\right]\right\}, \\ \varphi_{RW}(x,y) &= \text{arct}\left\{Im\left[A_R(x,y)e^{-igz(x,y)}\right]/Re\left[A_R(x,y)e^{-igz(x,y)}\right]\right\}. \end{aligned} \qquad (5.7)$$

In Fig. 5.6, we can see the retrieved wrapped phase, of the right and left side, after applying an average 3x3 convolution filter to smooth the data.

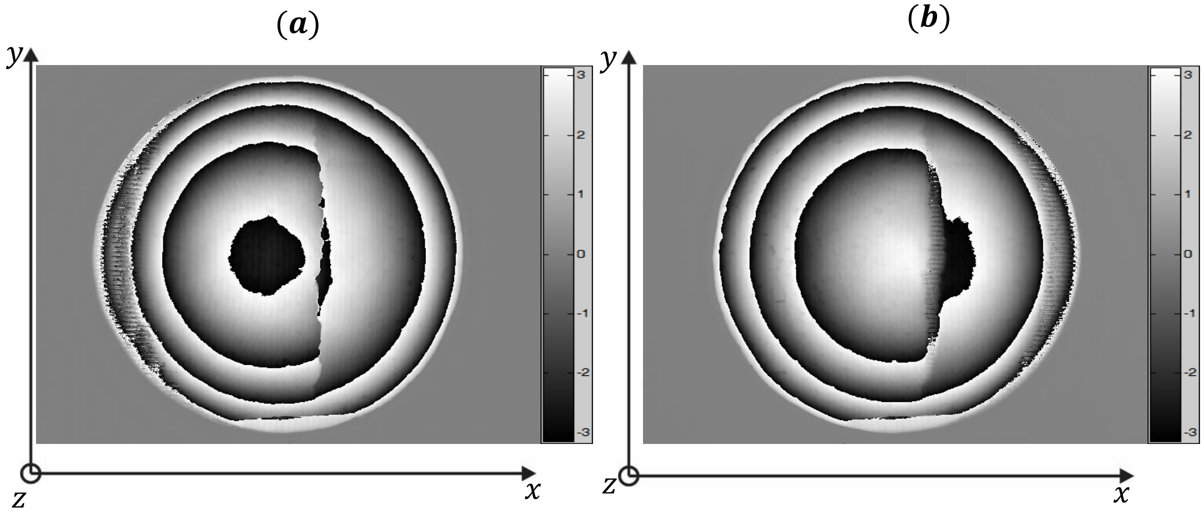

Fig. 5.6. - Wrapped phases obtained with illumination from the right projector (a) and with illumination from the left projector (b).

To show the limitation of the profilometry fringe setup of 1-camera and 1 projector, let's unwrap each image in Fig. 5.6 separately. The unwrapped phase using the flood-fill unwrapping algorithm on each wrapped phase map is shown in Fig. 5.7.

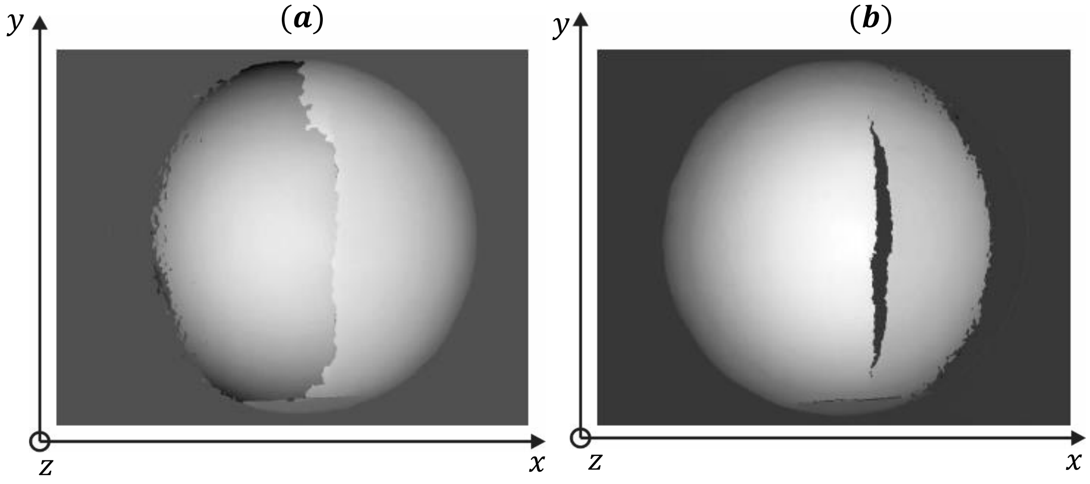

Fig. 5.7.-Unwrapped phases of each phase map: (a) right side and (b) left side.

Analyzing the unwrapped phase in Fig. 5.7, is evident that using a single projector is not possible to reconstruct the shape of discontinuous objects with shadows. The fracture of the half-sphere is not clearly seen in Fig. 5.7 (a) and in 5.7 (b) the area with self-occluding shadows remains undefined.

In summary, the produced shadows are seen as undefined phase areas with noise and different phase discontinuities. To compensate each shadow side, we can do a coherent sum of the phase of both demodulated fringe patterns as in Eq. 5.6. The resultant phase can be visualized in Fig. 5.8.

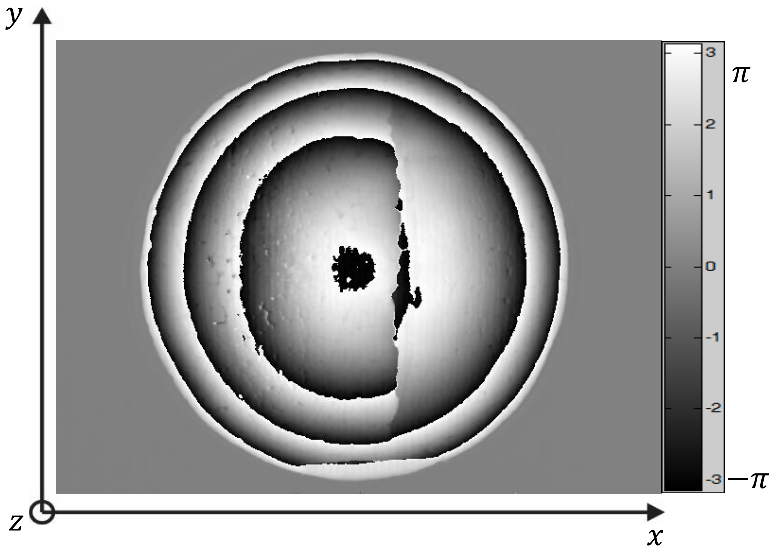

Fig. 5.8.-Resulting phase after the coherent sum of each phase map.

It’s worthy to distinguish that, with the co-phase technique, we can get rid of the undefined phase areas and where the fringe contrast is not optimal. Therefore, we get a phase map with better quality and easier to unwrap than a wrapped phase map using one single projector. Unwrapping the retrieved phase observed in Fig. 5.8 we obtain the 3D form of the object, which can be seen in Fig. 5.9.

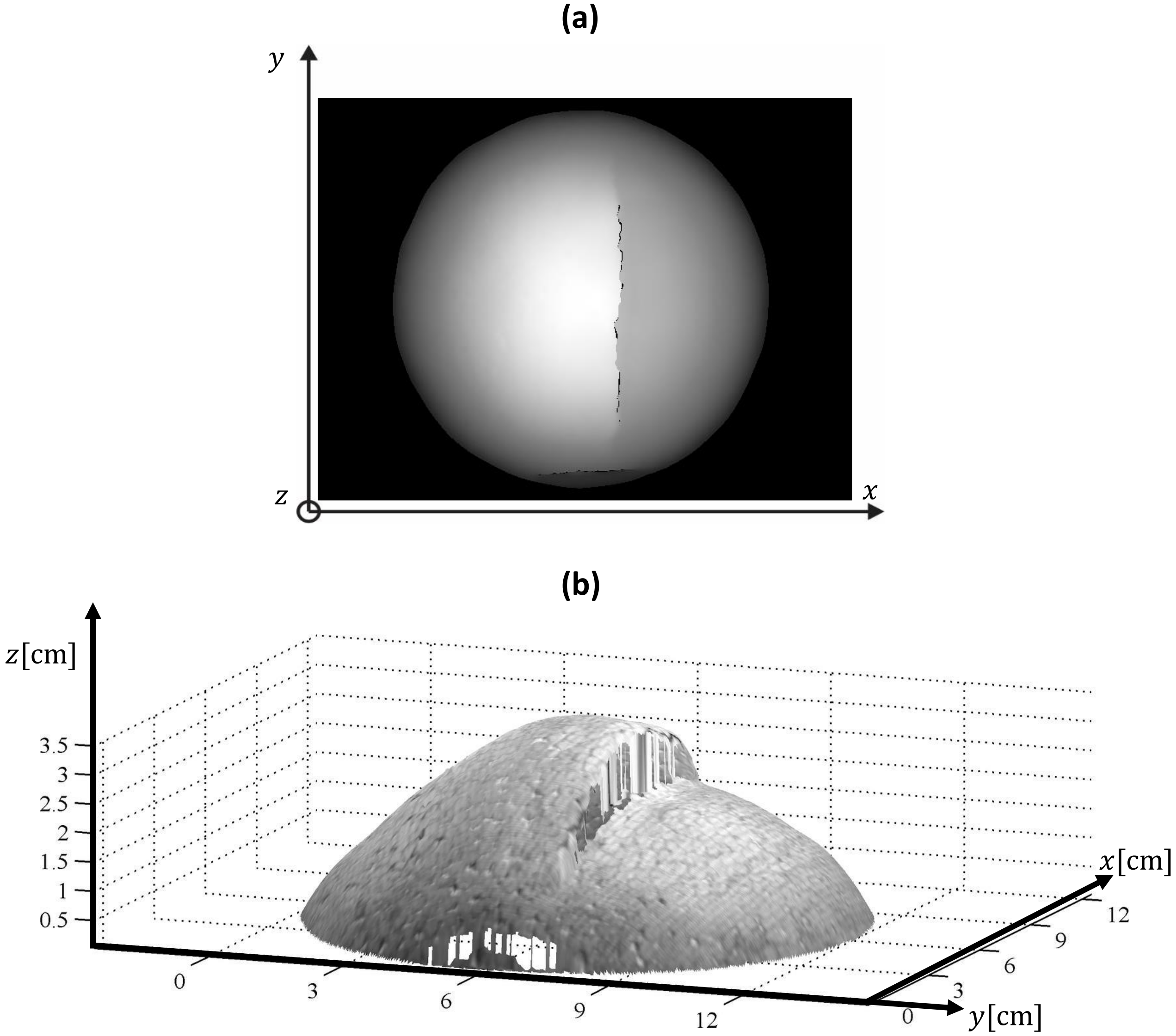

Fig. 5.9.-Reconstructed object using the co-phase technique with a four-step PSA: (a) unwrapped phase of the half-sphere and (b) 3D-shape of the half-sphere.

In conclusion, this is a powerful technique with an easy setup of basic profilometry. As we showed, one can get a phase map with better quality in comparison with the standard 1-projector and 1-camera arrangement.

5.2. On-axis fringe projection.

The implementation of this technique was inspired by the work of *Sicardi et al*. [34] in 2015. In the setup presented by *Sicardi,* a beam splitter is used to form the image of the object on the camera plane and at the same time the fringes are projected by a multimedia projector, making the angle between the camera and the projection 0°. Here is presented a different setup for the on-axis fringe projection. The places of the projector and the camera were switched in comparison to the preceding method, and also the beam splitter was change for a normal window glass (see Fig. 5.11).

In summary, with this technique the angle between the projection and the observation directions is zero. The system presents sensibility due to divergent projection which change the fringes frequency in each one of the normal planes along the z-axis. This means, that the system presents a frequency modulation due to the height of the measured object. The geometrical model of the frequency modulation caused by the changes in the z-axis of the object can be seen in Fig. 5.10.

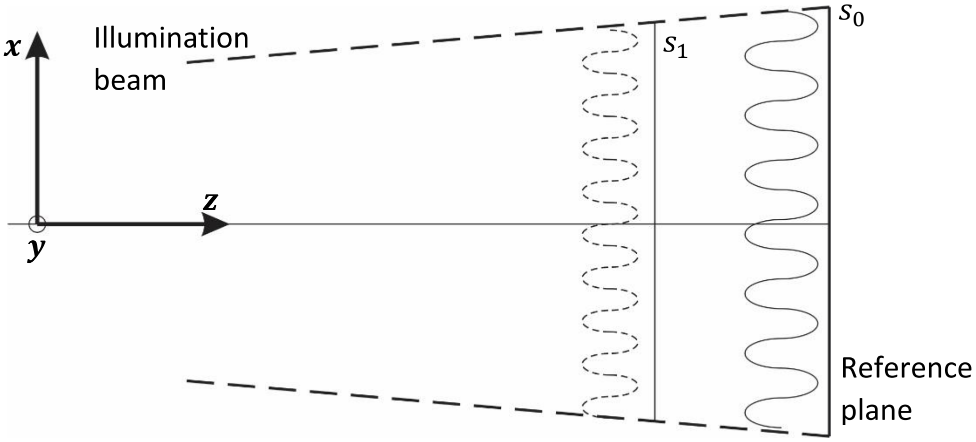

Fig. 5.10.-Schematic model of the frequency modulation of the fringes in on-axis projection.

This figure above, s_0 represents the reference plane. In this plane, fringes have their minimum frequency. As the object plane gets closer to the camera (like the plane s_1), and therefore to the projector beam, the frequency of the fringes increase. So, fringes projected onto the object will have a higher frequency than the reference plane behind the object.

The setup implemented for this technique consist in a CCD camera with resolution of 640x480 pixels, a fast opening illumination cone Dell projector with resolution 1024x768 pixels and a windows glass as beam splitter. The configuration of the on-axis arrangement is shown in Fig. 5.11.

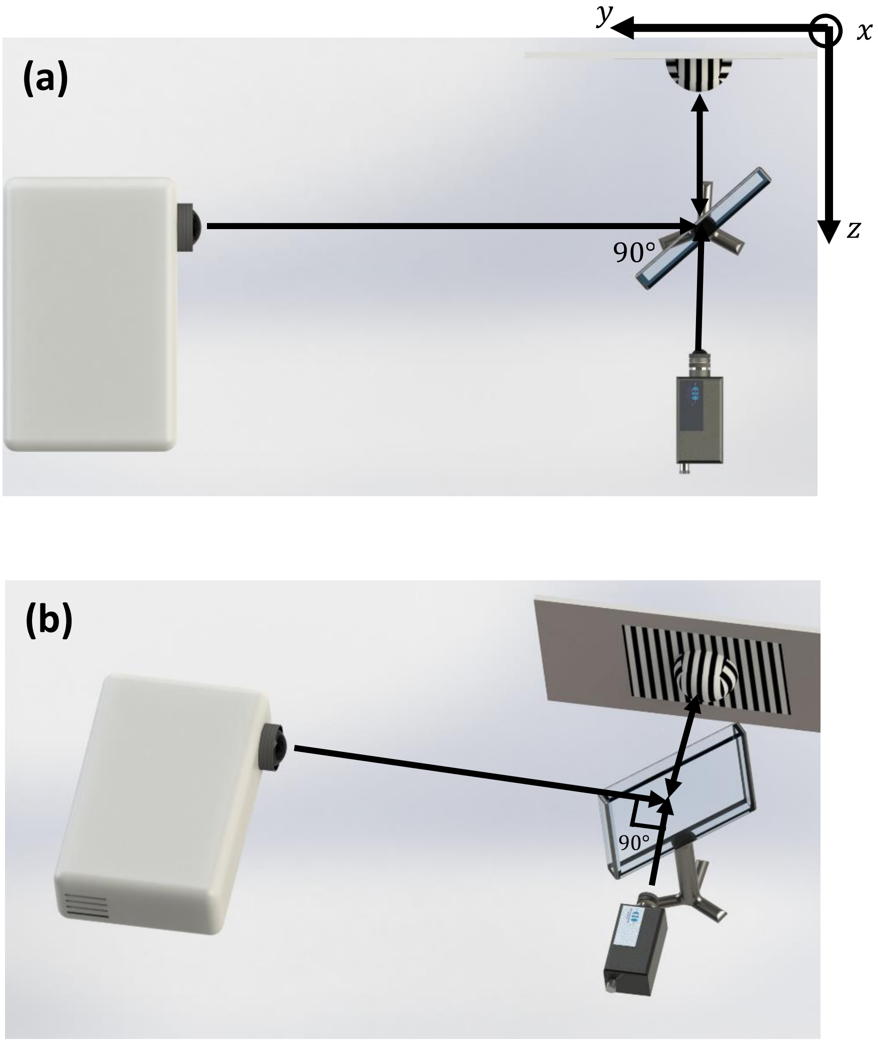

Fig. 5.11.-On-axis fringe profilometry setup. (a) Isometric view and (b) Top view.

Thanks to the use of a transparent window glass the camera can see the object directly through it. The projector's light beam is reflected by this window onto the object. Hence, the illumination axis and the view axis is the same, making 0° the angle between the camera and the projector. One advantage of this configuration is the elimination of shadows caused by a side incident light as in the case of the typical fringe projection setup.

As it was discussed before, the measuring is possible due the frequency modulation of the fringe pattern. Fig. 5.12 presents the images captured with this technique using a half-sphere as the object to measure. Likewise to the co-phase technique, the implemented demodulation method was a least-squares PSA but now with five-steps, every step with a phase shift of $^{2\pi}/_{4}$.

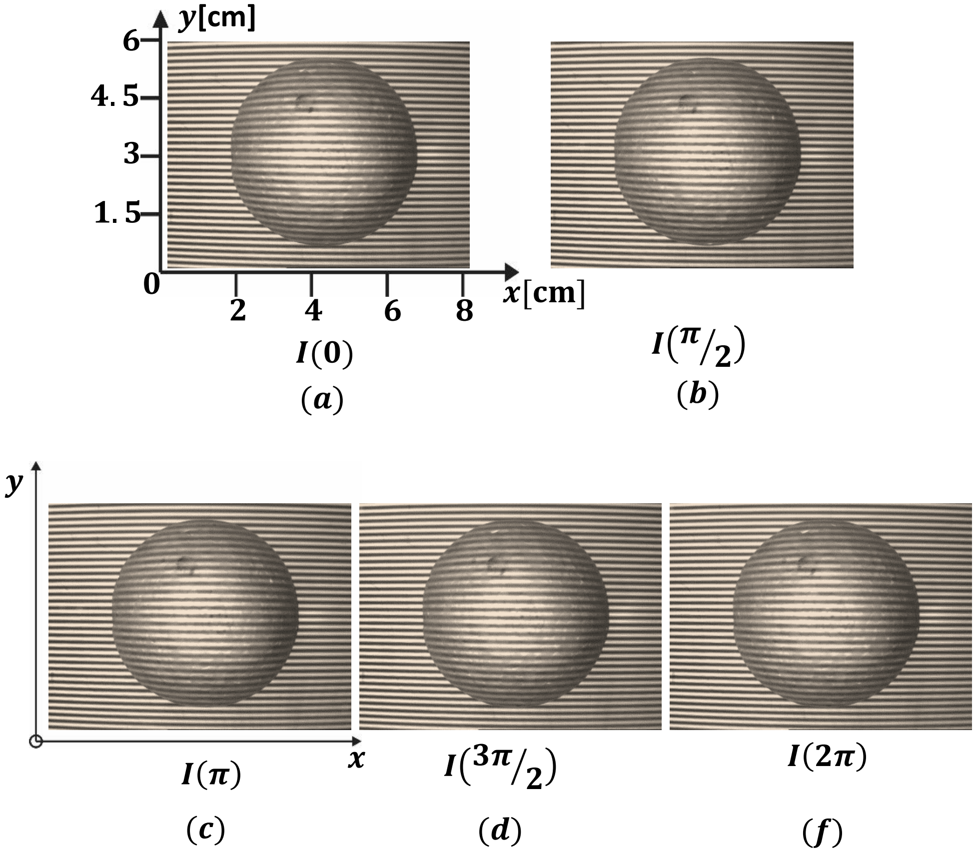

$I(0)$ (a)

$I(\pi/2)$ (b)

$I(\pi)$ (c)

$I(3\pi/2)$ (d)

$I(2\pi)$ (f)

Fig. 5.12.- (a-f) Captured images using a five-step PSA and a phase shift between steps of π/2, where is showed the frequency modulation of the fringes.

As it can be seen, the images do not present shadows where the phase won't be well defined. They present just some bright spots in the center of the object, but the fringes are still defined. This bright zone doesn't really affect the demodulation process as we will see later.

The five-step PSA was apply to the images as follow

$$A_0(x,y)\exp[i\hat{\varphi}(x,y)] = \sum_{n=0}^{4}\exp(i\omega_0 n)\, I_n; \qquad \omega_0 = {}^{2\pi}/_{5}. \tag{5.8}$$

Each image in Fig. 5.12 corresponds to the values of I_n in Eq. 5.6. Applying the angle function to the above equation we are able to retrieve the estimated wrapped phase of the interferogram. The computing phase is visualized in the next figure.

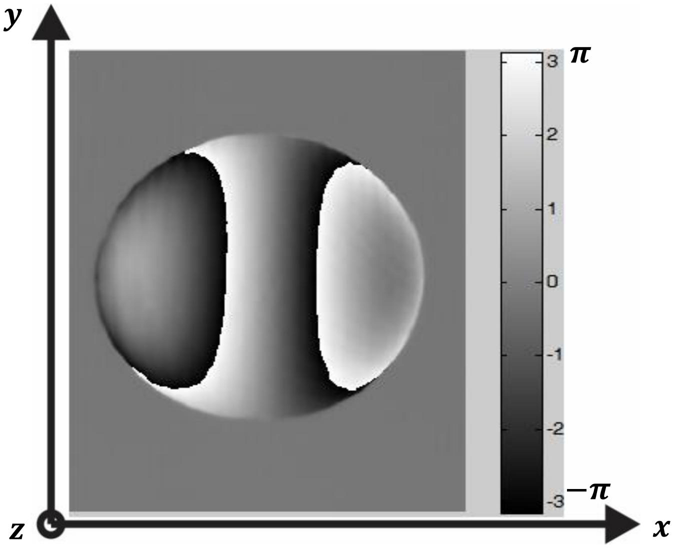

Fig. 5.13.-Retrieve phase of the object using on-axis technique.

The observed phase has mainly just two fringe contrasts, this means it change from $-\pi$ to π twice. It has a discontinuity at the center of the phase map, this can be demonstrated because the phase sign change from a positive value to a negative one. The next step to analyze this result is to unwrap the retrieved phase. To unwrap the phase in Fig. 512, the quality-guided flood-fill algorithm was used. Fig. 5.14 shows the unwrapped phase map.

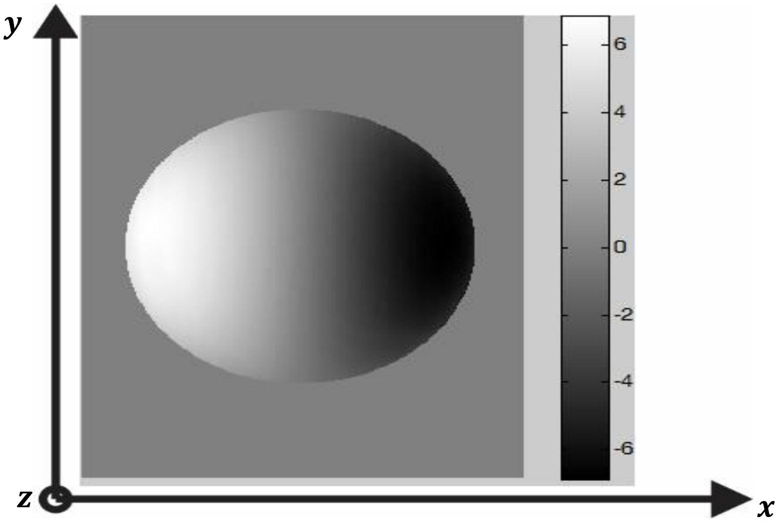

Fig. 5.14.-Unwrapped phase resulting with the on-axis technique.

With the unwrapped phase map is more evident the discontinuity at the center of the image. At the right side in Fig. 5.14, the phase got a low gray level value, and it increase while the x-axis of the image increase, that means the phase value get larger as it pass the center of the image. In order to get the real shape of the object, one must make the compensation of the height change in the phase value. We can increase the height value proportionally to the advance in the x-axis, but we will need to mask out the center of the image due to the 0 discontinuity. Therefore, we will need a compensating height algorithm and make an interpolation process at the center of the image to overtake that discontinuity.

5.3. Profilometry by line projection.

This technique was developed by *Servin et al.* [35] to make an easy reconstruction of discontinuous solids, also, due to just one strip-light is projected over the object, one can minimize the self-occluding shadow. This consists in the use of a CCD camera, a projector and a stepper motor with 1.8° per step, joined to a table to turn the object 360° over the azimuthal angle φ. The implemented setup is shown in Fig. 5.15.

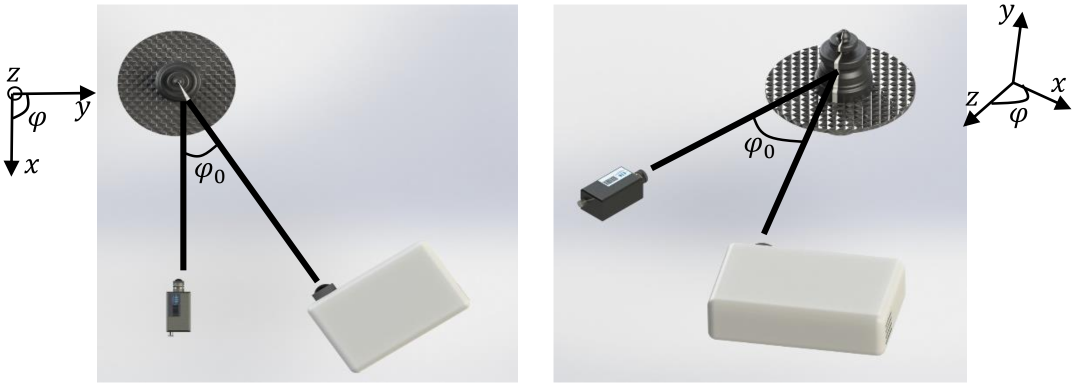

Fig. 5.15.-Configuration setup for the line projection profilometry.

The mathematical model for the intensity pattern of the single-line as imaged over the digitizing CCD camera plane $(y,z)\in\mathbb{R}^2$ is the following Gaussian irradiance,

$$G(y,z;\varphi)=\left[a(y,z;\varphi)+b(y,z;\varphi)\exp\left\{\frac{-[y-y(\varphi,z)]^2}{\sigma^2}\right\}\right]\prod(y); \qquad (5.9)$$
$$g=\sin(\varphi_0)\,,\varphi\in[0,2\pi].$$

Where $y(\varphi,z)$ is the projected line phase displacement. The profilometry sensitivity is given by $g=\sin(\varphi_0)$. The window function $\prod(y)$ is an indicator relation which may be expressed as,

$$\prod(y)=\left\{\begin{array}{ll}1 & if\ y\in[0,-\max[y(\varphi,z)]]\\ 0 & \text{Otherwise}\end{array}\right. . \qquad (5.10)$$

As seen in the previous Fig. 5.15, a single pixel line $y(\varphi,z)$ is projected onto one side of the object. The projected line is phase-modulated by the solid $y(\varphi,z)=\sin(\varphi_0)\,\rho(\varphi,z)$. Then, the CCD takes the image of $G(y,z;\varphi)$ and then the motor moves the object one single step $\Delta\varphi$. A picture is taken every time after the motor does a step, until the 360° of the object are scanned. This fringes are form using the window function of Eq. 5.10, with this is possible to make a box of valid data containing the single white line (white fringe) at the center and black pixels at the sides (black empty space). Taking an image of this box in every motor step and pasting them together, is possible to form a sequence of black and white lines as in a fringe pattern (see Fig. 5.17).

Once a set of N individual pixel lines images are taken at the discrete rotation angles $n\Delta\varphi$, we proceed to form the full fringe pattern $I(\varphi,z)$ of the digitized object $\rho=\rho(\varphi,z)$ in cylindrical coordinates as follow

$$I(\varphi,z)=G(\varphi,z)+(\varphi-\Delta\varphi,z)+\cdots+G(\varphi-(N-1)\Delta\varphi,z); \qquad \Delta\varphi=2\pi/N \tag{5.11}$$

The shape measurement by line projection was tested a ceramic piggy bank, as seen in Fig. 5.16.

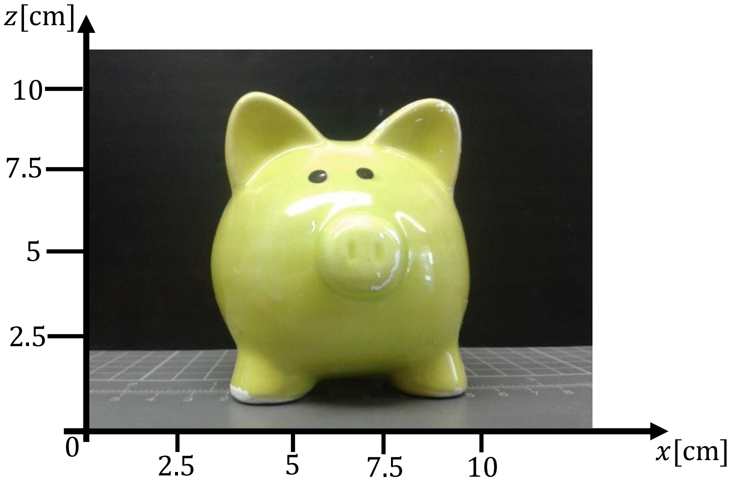

Fig. 5.16.- Objects to digitizing; a Piggy bank and.

The scanning total, a little more than 360°, consisted of 2600 x 480 pixels, composed of white fringes and constant black empty spaces.

The Fig. 5.17 shows the constructed carrier-fringe $I_p(\varphi,z)$ of this object by the projected line profilometer.

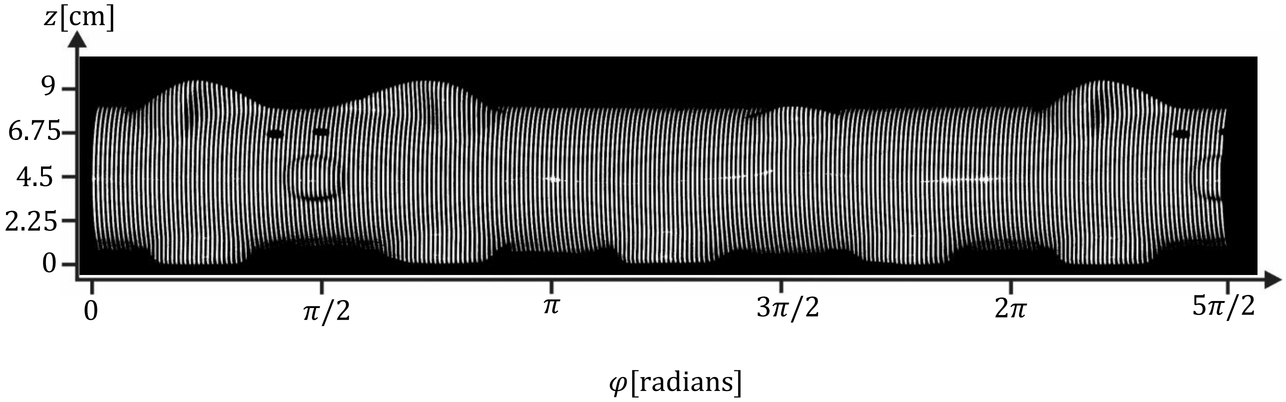

Fig. 5.17.-Fringe pattern construction from N digitized lines images.

As seen in the previous figure, the carrier-frequency fringe pattern is generated by assembling N-Gaussian lines side by side. The advantage of this scheme is that a single fringe pattern is enough to demodulate the solid's phase. The sum of N displaced irradiance lines $G(\varphi - n\Delta\varphi, z)$ forms the fringe pattern $I_p(\varphi, z)$ in Fig. 5.17. The first harmonics of $I_p(\varphi, z)$ is modeled by,

$$I_p(\varphi, z) = \sum_{n=0}^{N-1} G(\varphi - n\Delta\varphi, z) \approx a(\varphi, z) + b(\varphi, z)\cos[\omega_0\varphi + g\rho(\varphi, z)] \tag{5.12}$$

The 3D shape of the object is given by the demodulated phase $g\rho(\varphi, z)$. The spatial-carrier ω_0 of the constructed N fringes is numerically given by

$$\omega_0 = \frac{2\pi\ (\text{Number of lines in the } \varphi \text{ direction})}{\text{Numbers of pixels in the } \varphi \text{ direction}} \left(\frac{\text{radians}}{\text{pixels}}\right) \tag{5.13}$$

To obtain the searched phase $g\rho(\varphi, z)$, we are going to use the Fourier method, explained in chapter 3. So, taking the Fourier transform of the signal in Eq. (5.12), we get the spectrum of the phase-modulated fringe carrier (Fig. 5.18) as

$$\mathcal{F}[I_p(\varphi, z)] = A(\omega_\varphi, \omega_z) + C(\omega_\varphi - \omega_0, \omega_z) + C^*(\omega_\varphi + \omega_0, \omega_z). \tag{5.14}$$

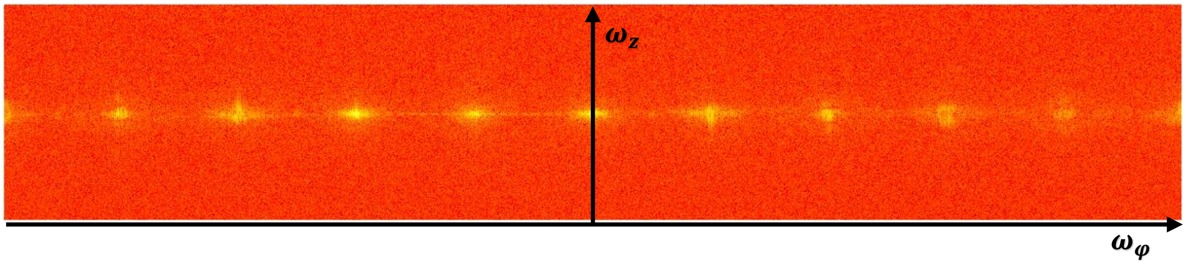

Fig. 5.18.-Frequency spectrum of the reconstructed fringe pattern.

Where $(\omega_\varphi, \omega_z) \in [-\pi, \pi] \times [-\pi, \pi]$ is the Fourier spectrum space corresponding to $I_p(\varphi, z)$ in cylindrical coordinates, and $C(\omega_\varphi, \omega_z) = \mathcal{F}\{(b(\varphi, z)/2)e^{-ig\rho(\varphi,z)}\}$. The central lobe is $A(\omega_\varphi, \omega_z)$, $C(\omega_\varphi - \omega_0, \omega_z)$ and $C^*(\omega_\varphi + \omega_0, \omega_Z)$ are the first right and left lobes respectively. The observed harmonics in Fig. 5.17 are mainly due to the use of light lines intensity profiles instead of a cosinuidal profile, like in the case of basic fringe projection profilometry.

Then, we need to move the lobe $C(\omega_\varphi - \omega_0, \omega_Z)$ to the origin of the spectrum, multiplying the signal $I_p(\varphi, z)$ by $e^{i\omega_0 * x}$. The following step is to compute its Fourier transform and apply a band pass filter (Fig. 5.19), in order to isolate the signal $C(\omega_\varphi, \omega_z)$.

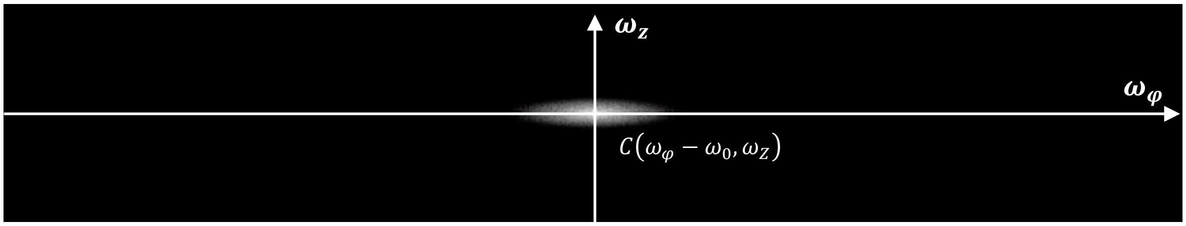

Fig. 5.19.-Spectrum of the signal $I_p(\varphi, z)$ after a band pass filter is applied.

After the first lobe is isolated, we use the inverse Fourier transform to obtaine the desired analytic signal as follow,

$$\mathcal{F}^{-1}[C(\omega_\varphi, \omega_z)] = \frac{b(\varphi, z)}{2} e^{ig\rho(\varphi,z)}. \tag{5.15}$$

Then, we can compute the angle of this complex function and get the wrapped phase $g\rho_W(\varphi, z) \in [-\pi, \pi]$, as seen in Fig. 5.20:

$$g\rho_W(\varphi, z) = \text{angle}\left[\frac{b(\varphi, z)}{2} e^{ig\rho(\varphi,z)}\right]. \tag{5.16}$$

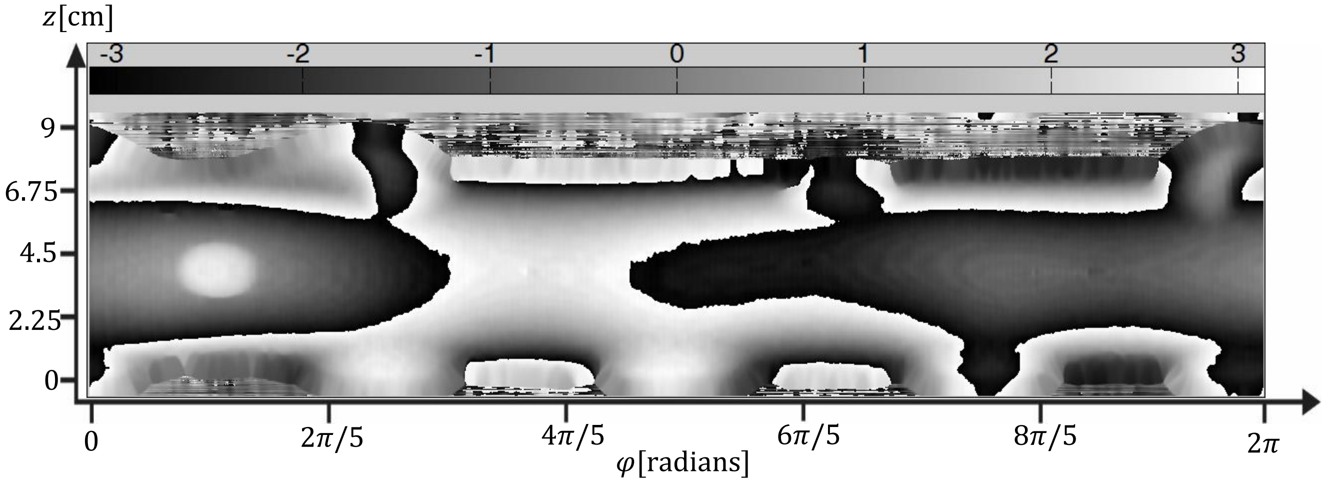

Fig. 5.20.-Wrapped phase of the analytic signal, belonging to the measured object.

Note that this wrapped phase is noisy in the zones that don't belong to the object. So, one must apply a mask, depending of the falling contrast in the magnitude of the signal. We assign a threshold to decide when the pixels have high or low phase data. Where there is low contrast, the mask take a 0 value, anywhere else the mask take a value of 1.

After the wrapped phase map is masked out, the following step is to cut the constructed fringe pattern to form the 360° of the object's full view. Fig. 5.21 shows the wrapped phase after applying the mask and cutting the exceeding pixels.

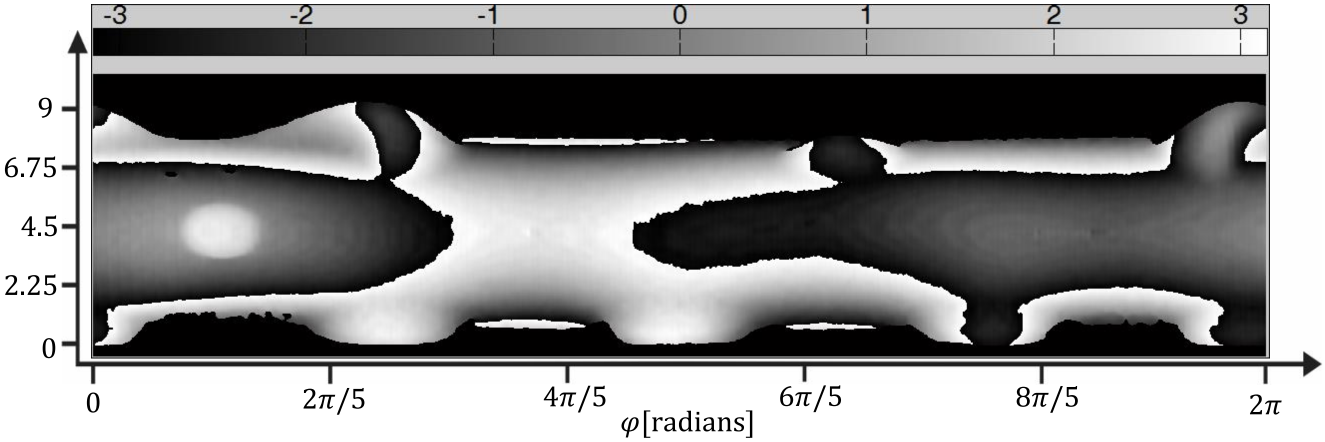

Fig. 5.21.-Wrapped phase of the analytic signal after the masking process.

Once obtained the wrapped phase, we can apply an unwrapping algorithm to get the phase $\hat{\varphi} \in [0,2\pi]$. The Fig. 5.22 shows the unwrapping phase after applying the quality-guided algorithm.

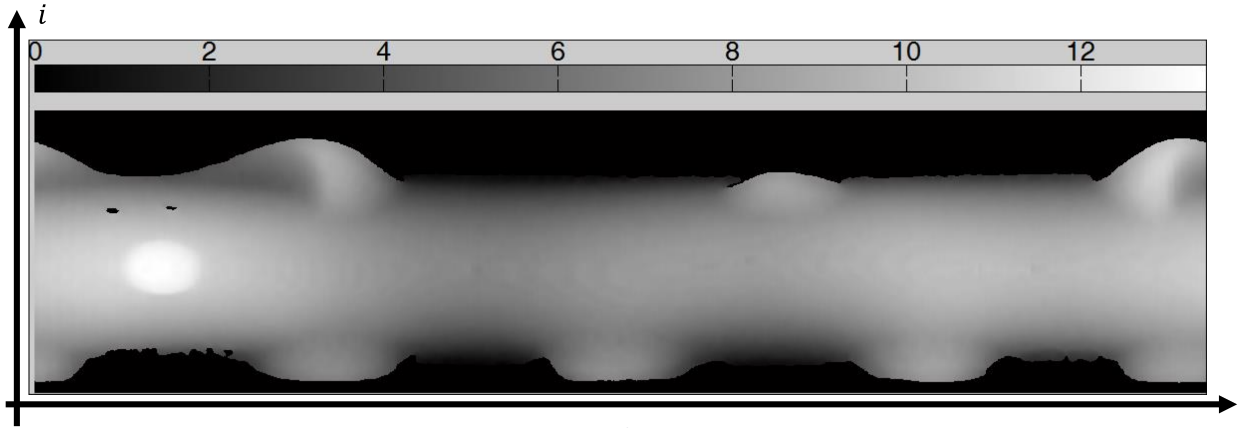

Fig. 5.22.-Unwrapped phase of the searched analytic signal.

The final step, is to change the cylindrical coordinates shown in Fig. 5.22 to form the 3D shape object and plot it in the software Matlab. Let us assign new axis labels corresponding to the figure above: i to the height and j to the length of the unwrapped phase map. So, we need a coordinate's conversion from cylindrical to rectangular, as follows

$$X(i,j) = -\hat{\varphi}(i,j) * \sin\left(\frac{2\pi j}{N}\right)$$
$$Y(i,j) == -\hat{\varphi}(i,j) * \cos\left(\frac{2\pi j}{N}\right)$$
$$Z(i,j) = -i - \frac{M}{2}. \tag{5.17}$$

Where N is the number of pixels in the length axis and M is the number of pixels in the height axis. After applying this conversion, we can plot the axis X, Y and Z with the *"surf"* instruction in Matlab. The reconstructed object is shown in the Fig. 5.23.

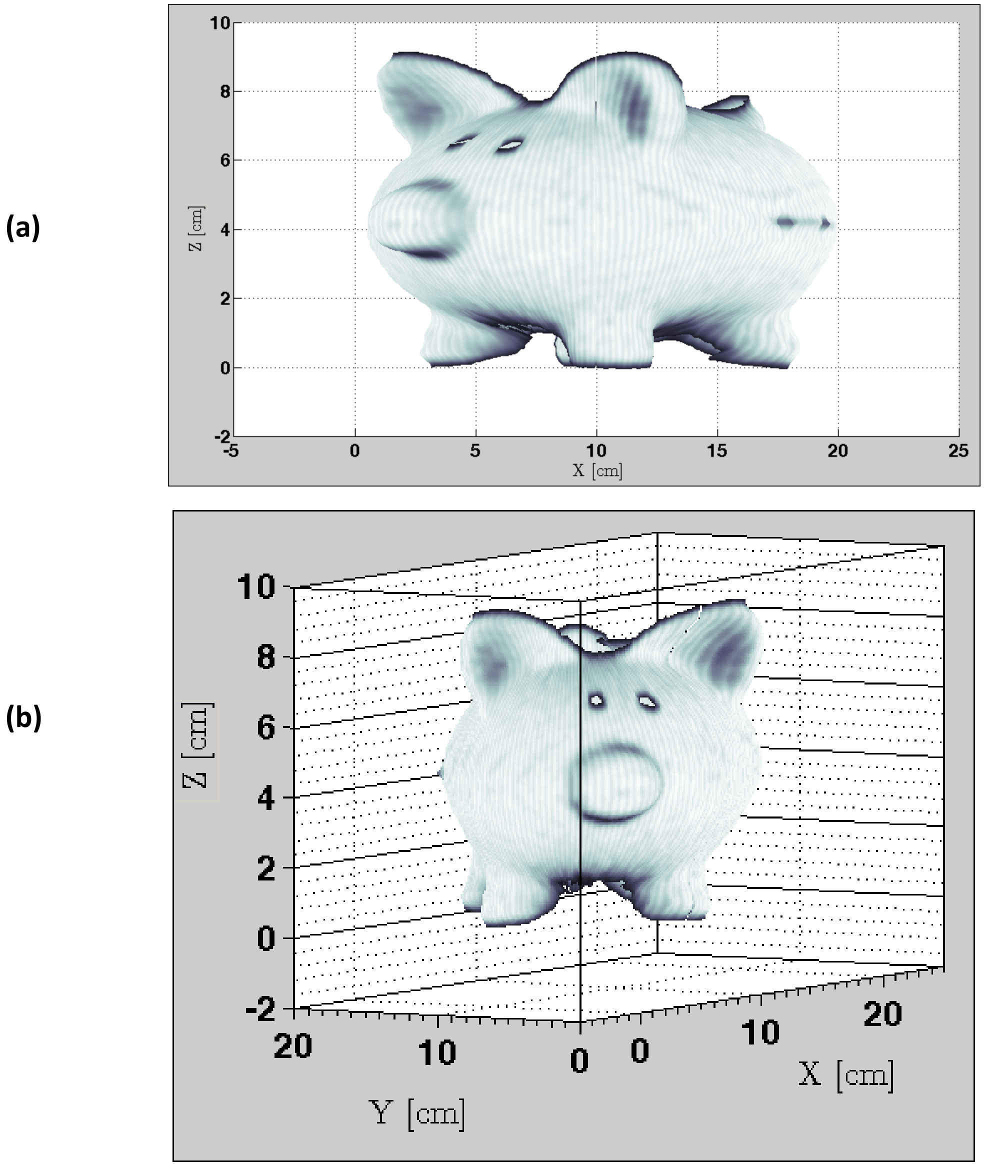

Fig. 5.23.- Different views of the digitized piggy bank using the 3D shape measurement by line projection: (a) lateral view and (b) front view.

Analyzing this first reconstruction, we note two points at the lateral sides of the object. This is due to the high reflective index of the object material, in this case shiny ceramic. But this isn’t an issue to reconstruct correctly the object.

6. Conclusions.

In this work, it was reviewed the theoretical background necessary for some structured light profilometry techniques. This includes topics of DSP, digital fringe analysis and fringe projection. Furthermore, was made an analize about the classic papers in fringe pattern profilometry, like the work of Takeda, and the recent publications in the fringe analysis research group at *Centro de Investigaciones en Optica.* The main contribution in this thesis is an algorithm, based in quality-guided and flood-fill method. Although this algorithm was too slow, it was able to unwrap some low-quality interferograms thanks to the quality guided and masking out invalid phase data. The slowness of this algorithm was due the fact that Matlab has a limited number of recursions in a single algorithm, and also, the stack function of this software has many limitations.

Mainly three techniques were replicated: co-phase fringe projection profilometry, on-axis fringe projection and 3D shape measurement by line projection.

The co-phase technique was confirmed to be a fast and easy way to digitize an object, eliminating self-occluding shadows. But, the alignment of the setup is a time-consuming. Also, one must look that the two projectors involved in the fringe projection needs to have the same projection beam angle, brightness, distance to the projection plane and the same angle respect to the camera. If these conditions are not fulfilled, one cannot do a correct mathematical sum between both sides (left and right) interferograms, resulting in

For the on-axis fringe projection, it was found that this technique reduces the self-occluding shadows on the object, but the object reconstruction has some troubles due to a discontinuity in the interferograms center. Therefore, with this technique is necessary to process more steps after the fringe demodulation.

In the case of the 3D profilometry by line projection, it was proven to be a relatively fast and easy method to digitalize solids. The fastness relativity is due that only one revolution of the object is needed to produce the open-fringes pattern, then it can be demodulate using the Fourier Method to retrieve the shape of the object. It has some limitations, like almost all other profilometry techniques, when the object has deep irregularities where the light cannot “see” through. However, the objects measured with this technique were reconstructed with a good quality, without deformation on its shape.

As a final conclusion, with the techniques here discussed, it were able to reconstruct the shape of different objects with different types of difficulties. When is necessary to do a full 360° reconstruction of the object, the profilometry by line projection is optimal to do a fast and accurate measurement of this object’s shape. In order to do this, the object will be turned on its own axis with a single line projected, and at the same time it will be scanned with a CCD camera, to finally be processed in a computer. In this case, the object needs to be reflective and opaque.

If the object present many irregularities in its shape, like fractures, the more efficient technique to use is the co-phase profilometry technique. Because this technique is able to eliminate the self-occluding shadows due to the object shape using two illumination on the sides of the object. The object to measure needs to be reflective to allow the camera see the deformed fringes.

References.

[1] J. Dirckx and J. Buytaert (eds). Optical measurement techniques for structures and systems. *Shaker publishing*. ISBN-978-90-423-0366 (2010).

[2] J. Yagnik, G. S. Siva, K. R. Ramakrishnan and L. K. Rao. 3D shape extraction of human face in presence of facial hair: a profilometric approach. *Proc. IEEE Region 10 Annual International Conference*. 4085277 (2009).

[3] G. Zhou, Z. Li, C. Wang and Y. Shi. A novel method for human expression rapid reconstruction. *Tsinghua science and technology,* 14, ISSN 1007-0214, 62-65 (2009).

[4] H. Lee, H. Cho and M. Kim. A new 3D sensor system for mobile robots based on Moire and stereo vision technique. *Proceedings of the international conference on intelligent robots and systems*, 1384-1389 (2006).

[5] F. Yuan, D. Song and L. Zeng. Measuring 3D profile and position of a moving object in large measuring range by using tracking fringe pattern. *Opt. Commun.* 196, 85-91 (2001).

[6] J. Burke, T. Bothe, W. Osten and C. Hess. Reverse engineering by fringe projection. *Proc. Of SPIE* 4778, 312-324 (2002).

[7] D. Hong, H. Lee, M. Y. Kim, H. Cho and J. II Moon. Sensor fusion of phase measuring profilometry and stereo vision for three-dimensional inspection of electronic components assembled on printed circuit boards. *App. Opt.* 48 (21), 4158-4169 (2009).

[8] M. Servin, J. A. Quiroga and J. M. Padilla. Fringe pattern analysis for optical metrology: theory, algorithms and applications. Wiley-VCH (2014).

[9] M. Takeda, H. Ina and S. Kobayashi. Fourier-transform method for fringe-pattern analysis for computer-based topography and interferometry. *J. Opt. Soc. Am.* 72(1), 156-160 (1982).

[10] M. Takeda and K. Mutoh. Fourier transform profilometry for the automatic measurement of 3-D object shapes. *App. Opt.* 22(24), 3977-3982 (1983).

[11] S. S. Gorti and P. Rastogi. Fringe profilometry techniques. *Opt. and Las. In Eng.* 48(2), 133-140 (2010).

[12] P. Rastogi and E. Hack (eds). Optical methods for solid mechanics: a full field approach. Wiley-VCH (2012).

[13] A. V. Oppenheim and R. W. Schafer. Digital signal processing. Prentice-Hall (1975).

[14] J. G. Proakis and D. G. Manolakis. Digital signal processing: principles, algorithms and applications. Prentice-Hall (1996).

[15] J. L. Marroquin, J. E. Figueroa and M. Servin. Robust quadrature filters. *J. Opt. Soc. Am.* 14(4), 779-791 (1997).

[16] J. H. Bruning, D. R. Herriott, J. E. Gallagher, D. P. Rosenfeld, A. D. White and D. J. Brangaccio. Digital wavefront measuring interferometer for testing optical surfaces and lenses. *App. Opt.* 13 (11). 2693-2703 (1974).

[17] Y. Ichioka and M. Inuiya. Direct phase detecting system. *App. Opt.* 11 (7). 1507-1515 (1972).

[18] M. Servin. Synchronous phase-demodulation of concentric rings Placido mires in corneal topography and wavefront aberrometry (theorical considerations). ArXiv e-prints.

[19] J. Millerd, N. Brock, J. Hayes, M. North-Morris, M. Novak and J. Wyant. Pixelated phase-mask dynamic interferometer. *Proc. SPIE.* 5531. 304-314 (2004).

[20] M. Servin and J. C. Estrada. Error-free demodulation of pixelated carrier frequency interferograms. *Opt. Exp.* 18 (17). 18492-18497 (2010).

[21] J. M. Padilla, M. Servin and J. C. Estrada. Synchronous phase-demodulation and harmonic rejection of 9-step pixelated dynamic interferograms. *Opt. Exp.* 20 (11). 11734-11739 (2012).

[22] A. Gonzales, M. Rivera, M. Servin, R. Legarda-Saenz, O. Dalmau and A. Martinez. Synchronous phase demodulation algorithm for conic carrier Hartmann topographer. *Opt. and Las. in Eng.* 157-162 (2014).

[23] K. H. Womack. Interferometric phase measurement using spatial synchronous detection. *Opt. Eng.* 23(4). 391-395 (1984).

[24] P. Carré. Installation et utilization du comparateur photoélectrigue et interferential du bureau international de poids ek mesures. *Metrologia*. 1. 13-23 (1966).

[25] C. J. Morgan. Least-squares estimation in phase-measurement interferometry. *Opt. Lett.* 7(8). 368-370 (1982).

[26] Y. Surrel. Design of algorithms for phase measurements by the use of phase stepping. *App. Opt.* 35(1). 51-60 (1996).

[27] D. W. Robinson. *Interferogram analysis: digital fringe pattern measurement techniques.* IOP Publishing Ltd. Cap. 6 (1993).

[28] K. Itoh. Analysis of the phase unwrapping algorithm. *App. Opt.* 21(14). 2470 (1982).

[29] S. Zhang, X. Li and S.-T. Yau. Multilevel-quality guided phase unwrapping algorithm for real-time three-dimensional shape reconstruction. *App. Opt.* 46(1). 50-57 (2007).

[30] M. Zhao, L. Huang, Q. Zhang, X. Su, A. Asundi and Q. Kemao. Quality-guided phase unwrapping technique: comparison of quality maps and guiding strategies. *App. Opt.* 55(33). 6214-6224 (2011).

[31] K. Chen, J. Xi, Y. Yu and J. F. Chicharo. Fast quality-guided flood-fill phase unwrapping algorithm for three-dimensional fringe pattern profilometry. *Proc. Of SPIE.* Vol. 7855 (2010).

[32] M. Servin, G. Garnica, J. C. Estrada and A. Quiroga. Coherent digital demodulation of single-camera N-projections for 3D-object shape measurement: Co-phase profilometry. *Opt. Exp.* 21(21). 24873-24878 (2013).

[33] M. Servin, G. Garnica and J. M. Padilla. Co-phased 360-degree fringe-projection profilometry of discontinuous solids using two projectors and a single camera. arXiv: http://arxiv.org/ftp/arxiv/papers/1408/1408.6463.pdf.

[34] A. Sicardi, J. C. Estrada, A. Martinez and G. Garnica. On axis fringe projection: A new method for shape measurement. *Opt. and las. In Eng.* 69. 29-34 (2015).

[35] M. Servin, M. Padilla and G. Garnica. Fourier phase-demodulation applied to strip-light 360-degrees profilometry of 3D solids; theoretical principles. arXiv: http://arxiv.org/ftp/arxiv/papers/1510/1510.04587.pdf.